JOURNAL OF GEOPHYSICAL RESEARCH, VOL. 114, A04216, doi:10.1029/2008JA013562, 2009

Cluster observations and numerical modeling of energy-dispersed ionospheric H^+ ions bouncing at the plasma sheet boundary layer

J. M. Bosqued,[1] M. Ashour-Abdalla,[2,3] T. Umeda,[4] M. El Alaoui,[2] V. Peroomian,[2] H. U. Frey,[5] A. Marchaudon,[6] and H. Laakso[7]

Received 3 July 2008; revised 13 January 2009; accepted 24 February 2009; published 28 April 2009.

[1] The Cluster mission offers a unique opportunity to investigate the origin of the energy-dispersed ion structures frequently observed at 4.5–5 R_E altitude in the auroral region. We present a detailed study of the 14 February 2001 northern pass, characterized by the successive observation by three spacecraft of a series of energy-dispersed structures at ~72–75° ILAT in a region of poleward convection. Equatorward, the satellites also observed a localized, steady, and intense source of outflowing energetic (3–10 keV) H^+ and O^+ ions. These substructures were modeled by launching millions of H^+ ions from this ionospheric source and following them through time-dependent electric and magnetic fields obtained from a global MHD simulation of this event. Despite the complexity of ion orbits, the simulations showed that a large number of ions returned to the Cluster location, poleward of their source, in a number of adjacent or overlapping energy-latitude substructures with the correct dispersion. The first dispersed echo was unexpectedly generated by ''half-bouncing'' ions that interacted with the current sheet to return to the same hemisphere. The time-shifted observations made by two Cluster (SC1 and SC3) spacecrafts were correctly reproduced. Almost all the ions returning to the spacecraft underwent a ~2–5 keV nonadiabatic acceleration at each interaction with the current sheet in a very confined resonant region. This acceleration explains the overall energy increase from one structure to the next. This event confirms the importance of the ionospheric source in populating bouncing ion clusters within the magnetosphere, even at high latitudes.

Citation: Bosqued, J. M., M. Ashour-Abdalla, T. Umeda, M. El Alaoui, V. Peroomian, H. U. Frey, A. Marchaudon, and H. Laakso (2009), Cluster observations and numerical modeling of energy-dispersed ionospheric H^+ ions bouncing at the plasma sheet boundary layer, *J. Geophys. Res.*, *114*, A04216, doi:10.1029/2008JA013562.

1. Introduction

[2] For decades now energy-dispersed ion structures have been observed in many regions of the magnetosphere, ever since their first observation at geosynchronous orbit by ATS-5 & 6 [*Quinn and McIlwain*, 1979] and their subsequent interpretation as time-of-flight effects after impulsive injection [*Quinn and Southwood*, 1982]. They were first observed by the DE1-2 [*Winningham et al.*, 1984] and Aureol-3 spacecraft [*Bosqued et al.*, 1986a] in the low altitude nightside auroral region. Since then, energy-dispersed 1–15 keV ion bouncing beams have been considered to be basic signatures that remotely provide invaluable information about acceleration and transport processes in the near or distant magnetosphere. These ions, which bounce between conjugate hemispheres, have again been observed in the form of numerous types of single or multiple dispersed bands, at midlower altitudes (~10.000 km) by Akebono [*Hirahara et al.*, 1996, 1997], at altitudes of 2–3 R_E above the auroral region by the Interball satellite [*Sauvaud et al.*, 1999; *Popescu et al.*, 2002; *Sauvaud and Kovrazhkin*, 2004] and at altitudes ranging from 4–7 R_E by the Polar satellite [*Lennartsson et al.*, 2001]. Clearly associated with substorms, all these recurrent and sporadic dispersed ion beams were interpreted as time-of-flight dispersed structures. At the near-Earth equatorial plane (~10 R_E) Geotail also observed bouncing ion clusters coincident with the dipolarization phase of a substorm [*Kazama and Mukai*, 2003, 2005]. More recently, bouncing ions injected from the far-distant magnetotail have been

[1]Centre d'Etude Spatiale des Rayonnements, Centre National de la Recherche Scientifique, Toulouse, France.
[2]Institute of Geophysics and Planetary Physics, University of California, Los Angeles, California, USA.
[3]Department of Physics, University of California, Los Angeles, California, USA.
[4]Geospace Research Center, Solar-Terrestrial Environment Laboratory, Nagoya University, Nagoya, Aichi, Japan.
[5]Space Sciences Laboratory, University of California, Berkeley, California, USA.
[6]Laboratoire de Physique et Chimie de l'Environnement, Centre National de la Recherche Scientifique, Orleans, France.
[7]Space Science Department, European Space Research and Technology Centre, European Space Agency, Noordwijk, Netherlands.

0148-0227/09/2008JA013562$09.00

identified by Cluster at high latitudes as energy-dispersed ion structures [*Keiling et al.*, 2005].

[3] Most, if not all, of these events were interpreted in terms of time of flight effects, and the systematic ion source was inferred to be the equatorial magnetotail, located at distances extending from $\sim$20–110 R_E. Although ionospheric upflowing ions were first seen more than 3 decades ago, with the polar orbiting S3/3 satellite making the first *in situ* observations at altitudes of 1000–8000 km [*Shelley et al.*, 1972, 1976], they have surprisingly received considerably less attention as a potential source for bouncing ions and, thus as a credible alternative to the magnetotail ion source. Nevertheless, it is clearly established that upflowing ion beams (UFIs) leave the terrestrial ionosphere and are a common feature on auroral field lines. These upflowing ions have been observed by numerous spacecraft at all local times and at altitudes, extending from 400 to 30,000 km [*Whalen et al.*, 1978; *Yau et al.*, 1984; *Ghielmetti et al.*, 1978; *Klumpar*, 1979; *Kondo et al.*, 1990, and references therein]. Upflowing ion distributions have been categorized into three families, field-aligned (''beams''), transversely peaked (''conics''), and hybrids (when conic and field-aligned features are both present). Field-aligned 1–10 keV beams were observed to be more frequent in the 21–24 H MLT sector, during quiet periods [*Kondo et al.*, 1990], and probably resulted from the action of an upward, quasistatic, parallel electric field [*Mozer et al.*, 1980]. More recently, other evidence was produced by comparing ion beam energies with the inferred parallel potential drops [e.g., *Marklund*, 1993], and by comparing the characteristic ion beam energy to the integration of the perpendicular electric field along the spacecraft path [*McFadden et al.*, 1998]. Moreover, parallel acceleration resulting from a quasistatic potential drop has also been clearly demonstrated by comparative studies of observations from two spacecraft [*Reiff et al.*, 1986, 1988; *Schriver et al.*, 2003]. To summarize, accelerated ionospheric ion beams, which have been observed to flow outward into the magnetosphere in the dusk to midnight auroral oval, appear to constitute significant sources for ring current, plasma sheet, and, more relevantly, bouncing ions.

[4] This alternative, i.e., an ionospheric source for bouncing ions, was initially explored as a possible interpretation of DE1 observations at low altitudes [*Winningham et al.*, 1984]. Later, *Bosqued et al.* [1986a] interpreted energy-dispersed ion structures (decreasing energy with decreasing latitude) as a signature of bouncing ions being ejected from an ionospheric source and subsequently dispersed in space (latitude) by the $\mathbf{E} \times \mathbf{B}$ magnetospheric convective ''filter.'' This study was the first to establish the correlation between each observed ion structure and the inverted-V electron structure observed in the vicinity. Such structures are direct evidence of low-altitude, field-aligned acceleration in a confined, narrow region (in latitude). Akebono [*Hirahara et al.*, 1996, 1997] observed multiple and overlapped energy-dispersed signatures at higher altitudes (7400–9600 km), together with <3 keV upflowing ion beams. The investigators interpreted the ordering of the energy bands as resulting from strong azimuthal $\mathbf{E} \times \mathbf{B}$ drift effects acting on multiple bouncing ionospheric beams.

[5] High-speed ion beams are also common in the plasma sheet boundary layer (PSBL) that separates the plasma sheet from the tail lobes [*Scarf et al.*, 1973; *DeCoster and Frank*, 1979; *Möbius et al.*, 1980, 1983; *Andrews et al.*, 1981; *Williams*, 1981; *Forbes et al.*, 1981; *Eastman et al.*, 1984, 1985; *Parks et al.*, 1998; *Ashour-Abdalla et al.*, 2008]. Within this layer of 1–2 R_E thickness the higher energy earthward-directed beams are localized at the lobeward edge of the PSBL, and lower energy beams, as well as tailward-directed beams equatorward of this boundary [*Takahashi and Hones*, 1988; *Parks et al.*, 1998; *Ashour-Abdalla et al.*, 2008]. A number of mechanisms have been suggested for the formation and layering of these beams, including nonadiabatic acceleration in the neutral sheet [*Speiser*, 1965; *Lyons and Speiser*, 1982; *Büchner and Zelenyi*, 1986; *Ashour-Abdalla et al.*, 1992], ejection from a distant reconnection line [*Cowley*, 1980; *Birn et al.*, 1986; *Schindler and Birn*, 1987; *Birn and Hesse*, 1991], and resonance between ions and kinetic Alfvén waves [*Hasegawa*, 1987; *Moghaddam-Taaheri et al.*, 1991].

[6] The energy-dispersed ion beams found in the PSBL have been also observed at lower altitudes. Using observations from the low-altitude AUREOL-3 satellite, *Bosqued* [1987] first found a second family of precipitating ions in a very narrow region just $\leq 0.5^\circ$ latitude equatorward of the polar cap boundary manifested clear energy-latitude (Λ) dispersion always of the form $\Lambda \propto 1/(E)^{1/2}$ with the highest-energy ions occurring at the highest latitudes. Tens of examples of these velocity-dispersed ion structures (VDIS) were described by *Zelenyi et al.* [1990] and *Bosqued et al.* [1993]. Particle tracing simulations carried out by *Ashour-Abdalla et al.* [1992, 1993] to try to investigate the VDIS origin first demonstrated the spatial effect proposed by *Zelenyi et al.* [1990]. The energy gained by plasma mantle ions through nonadiabatic Speiser orbits [*Speiser*, 1965] was inversely proportional to B_z, the vertical component of the local magnetic field, so that the most energetic ions were accelerated far in the tail and appeared near the PSBL-lobe separatrix. Although using two-dimensional reductions of empirical magnetic field models, this early simulation work produced VDIS in good agreement with the observations, as well as ''echoes,'' formed by the reflection of these beams at the ionosphere and subsequent interaction with the tail current sheet, 2–3° equatorward of the initial structure [*Ashour-Abdalla et al.*, 1992; *Bosqued et al.*, 1993]. Moreover, they found that nonadiabatic motion in the equatorial current sheet acted to separate ions into two distinct populations, according to the downtail location of their interaction with the current sheet. The ions were strongly accelerated only at ''resonant'' points, to generate layers of PSBL substructures and subsequent VDIS ''beamlets,'' while, in between, the remainder of the injected ions were scattered and formed the central plasma sheet (CPS). All these predictions, including echoes and beamlets, were subsequently observed at low altitudes [*Bosqued et al.*, 1993]. Further details on this resonant process were given by *Ashour-Abdalla et al.* [1995]. The new, multiple spacecraft Cluster observations have renewed the interest in dispersed beams and the to date the clearest reported example of VDIS [*Keiling et al.*, 2004a] was characterized by the classical dispersed ion signature with highly detailed beamlets embedded within. In recent work, *Ashour-Abdalla et al.* [2005] traced VDIS ions observed during that event backward in time in three-dimensional electric and magnetic

fields obtained from global magnetohydrodynamic (MHD) simulations and found that observed VDIS were generated in a large region of nonadiabatic motion, called the ''stochastic sea,'' just earthward of the neutral line.

[7] Thus except during the initial low (<2 R_E) altitude observations, the causal ion source of the resulting energy-dispersed structures was inferred, but not actually observed by the same spacecraft. This paper presents a unique and exciting example of multiple energy-dispersed ion structures encountered in the near-Earth (~4.5 R_E altitude) plasma sheet boundary layer (PSBL) by the Cluster Ion Spectrometers (CIS) on 14 February 2001, when the fleet of Cluster spacecraft crossed the northern auroral oval from south to north. The observations presented here are from three Cluster spacecraft (SC1, SC3, and SC4) and perfectly illustrate how multipoint measurements can be decisive in removing the space versus time ambiguities that continue to hinder efforts to interpret such dispersed structures. The spacecraft, separated by ~100 s in time, made similar observations of energy-dispersed structures that were time shifted; when reorganized in space (i.e., in latitude), the observations are identical. The simultaneous observation of a potential ion source of ionospheric outflowing ions, together with the returning echoes after these ions propagate and bounce along field lines, make this event unique. In such a case, as in active experiments that have been widely carried out in space, when particles of known properties are injected in one place along a field line, conjugate or same hemisphere effects (e.g., observation of a returning beam) can give decisive information and place strong constraints on the magnetospheric convection, as well as on the acceleration processes occurring at some place along the particle trajectory.

[8] Interest in this unique event is not new and has motivated a number of previous analyses [*Keiling et al.*, 2004a; *Sauvaud and Kovrazhkin*, 2004]. These studies interpreted observations in terms of time-of-flight effects acting on particles ejected from multiple equatorial sources and inferred that the successive energy-dispersed structures were time dispersions. In a preliminary paper [*Bosqued et al.*, 2006] we demonstrated that the incomplete analysis of the full set of experimental data, and particularly the missing key observation of the local, very intense, ionospheric ion source, invalidated this interpretation. In the present paper we go a step further by presenting the full set of data and the numerical simulations of the full event. In order to determine the actual destiny of ions ejected from the ionospheric source, to gain deeper insight into the physics of transport and possible acceleration, and thus definitively validate our interpretation of an ionospheric origin for the observed structures, we quantitatively modeled the magnetosphere by using a coupled magnetosphere-ionosphere, global time-dependent MHD code driven by the actual interplanetary (magnetic field, solar wind) parameters from the ACE spacecraft during this event. In spite of a number of well-known limitations, MHD simulations represent the state of the art in reproducing the global topology of the magnetosphere, the global electric and magnetic fields, as well as the global convection pattern [e.g., *Raeder et al.*, 1995, 1998; *Ashour-Abdalla et al.*, 1999, 2000, 2002; *El-Alaoui*, 2001; *El-Alaoui et al.*, 2008]. One shortcoming of MHD codes is that they lack some of the details of the reconnection process during the growth and expansion phases of substorms. However, since this 14 February 2001 event occurs after the recovery phase of a substorm event, the MHD simulation should and does give a rather reasonable and accurate time-dependent global topology of the magnetosphere. In addition, the Large-Scale Kinetic (LSK) model in its most recent version [*Ashour-Abdalla et al.*, 2005, 2008] was used to follow millions of upward moving H^+ ions ejected from an ionospheric source, through the time-dependent electric and magnetic fields provided by the MHD model. Virtual Cluster spacecraft were moving in the model at the correct location for collecting returning ions.

[9] This paper is organized in the following manner. Section 2 briefly describes Cluster's orbit and instruments, and section 3 presents the prevailing interplanetary and magnetospheric conditions, including the convection pattern produced by the SuperDARN radar chain. Section 4 presents a survey of the Cluster multi-instrument data provided by the SC1, SC3, and SC4 spacecraft. Details of the global MHD and LSK tools and the obtained results are in section 5. Finally, section 6 discusses the limitations of the technique used in this study, examines alternative interpretations and summarizes various aspects of the generation of energy-dispersed structures observed during this event.

2. Cluster Orbit and Instrumentation

[10] The four identical CLUSTER spacecraft move along an elliptical orbit with a perigee of 4 R_E, an apogee of 19.6 R_E, a period of ~58 h, and an inclination of 90°. When the apogee is around noon and in the solar wind, the Cluster spacecraft approach from the southern lobe, cross first the southern auroral region, next the radiation belts (near perigee), and then pass from the radiation belts into the northern lobe through the northern auroral region and the low-altitude extent of the PSBL at an altitude of 4–5 R_E. Near perigee, the usual tetrahedron configuration changes to a string-of-pearls configuration. For the present event, SC1 was in the lead, followed by SC3 and SC2, and finally by SC4 and their successive poleward tracks, mapped into the postmidnight ionosphere, were roughly superposed onto the 01.30–01.50 MLT meridian.

[11] In this paper we use particle data provided by the Cluster Ion Spectrometers (CIS), fully described by *Rème et al.* [2001], electron data from the Plasma Electron And Current Experiment (PEACE [*Johnstone et al.*, 1997]), electric field data from the Electric Field and Wave (EFW) instrument [*Gustafsson et al.*, 2001], magnetic field data from the Fluxgate Magnetometers (FGM [*Balogh et al.*, 2001]), and the drift velocity from the Electron Drift Instrument (EDI [*Paschmann et al.*, 2001]). As a result of an unidentified electronic failure, both CIS instruments on Cluster spacecraft SC2 were switched off. The observations presented in this study include CIS-2/HIA data from spacecraft SC1 and SC3 and CIS-1/CODIF data from spacecraft SC4 (CIS-2/HIA was switched off on SC4).

3. Interplanetary Conditions, Space, and Ground-Based Measurements

[12] The preliminary *AE* index obtained from the World Data Center for Geomagnetism in Kyoto is plotted in Figure 1

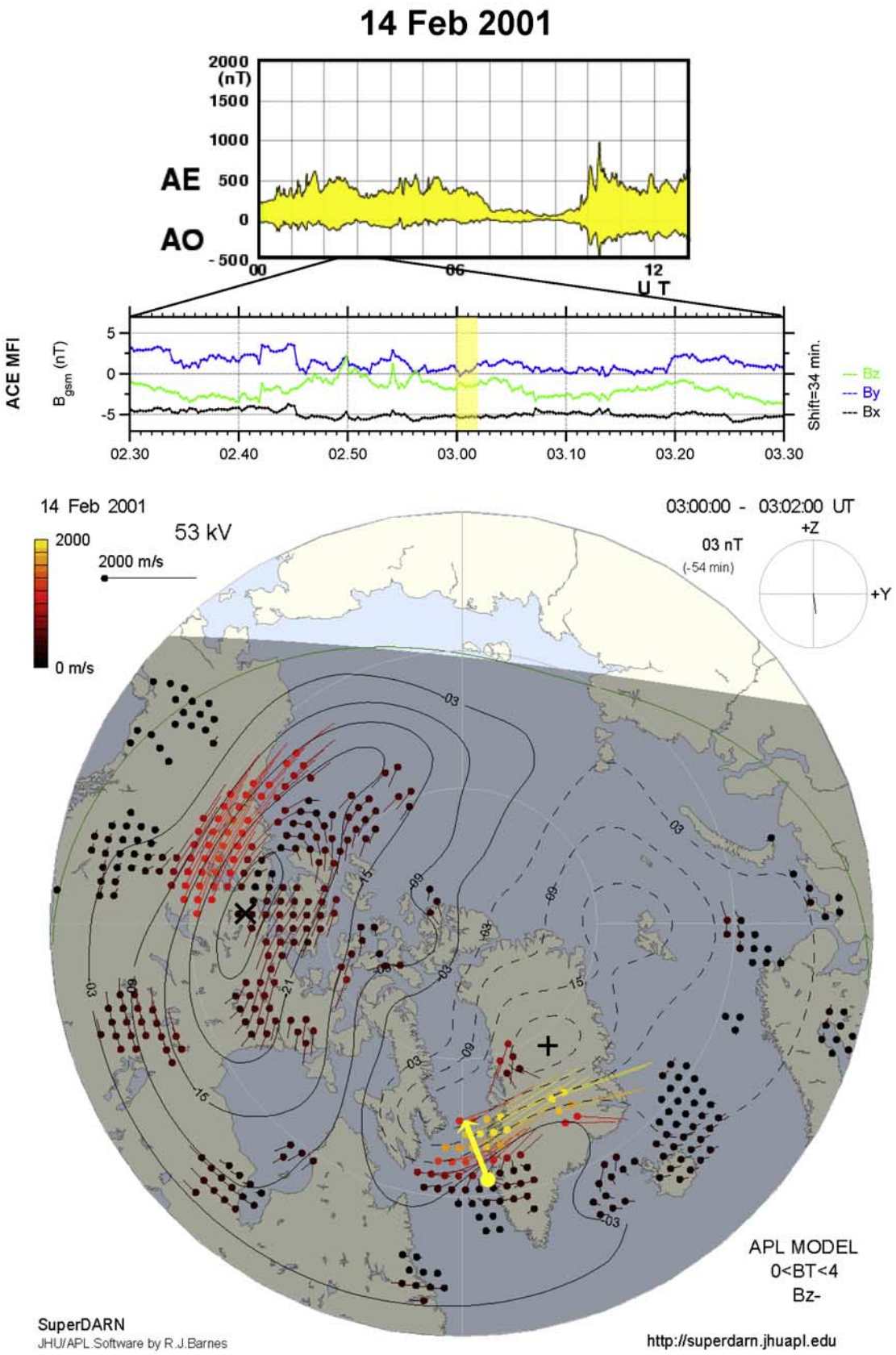
14 Feb 2001
2000 (nT)
1500
1000
AE
500
0
AO
- 500
00
06
12
U T
ACE MFI
B_{gsm} (nT)
5
0
-5
Shift=34 min.
Bz
By
Bx
02.30
02.40
02.50
03.00
03.10
03.20
03.30
14 Feb 2001
53 kV
2000
2000 m/s
0 m/s
03:00:00 - 03:02:00 UT
+Z
03 nT
(-54 min)
+Y
APL MODEL
0<BT<4
Bz-
SuperDARN
JHU/APL Software by R.J.Barnes
http://superdarn.jhuapl.edu

Figure 1

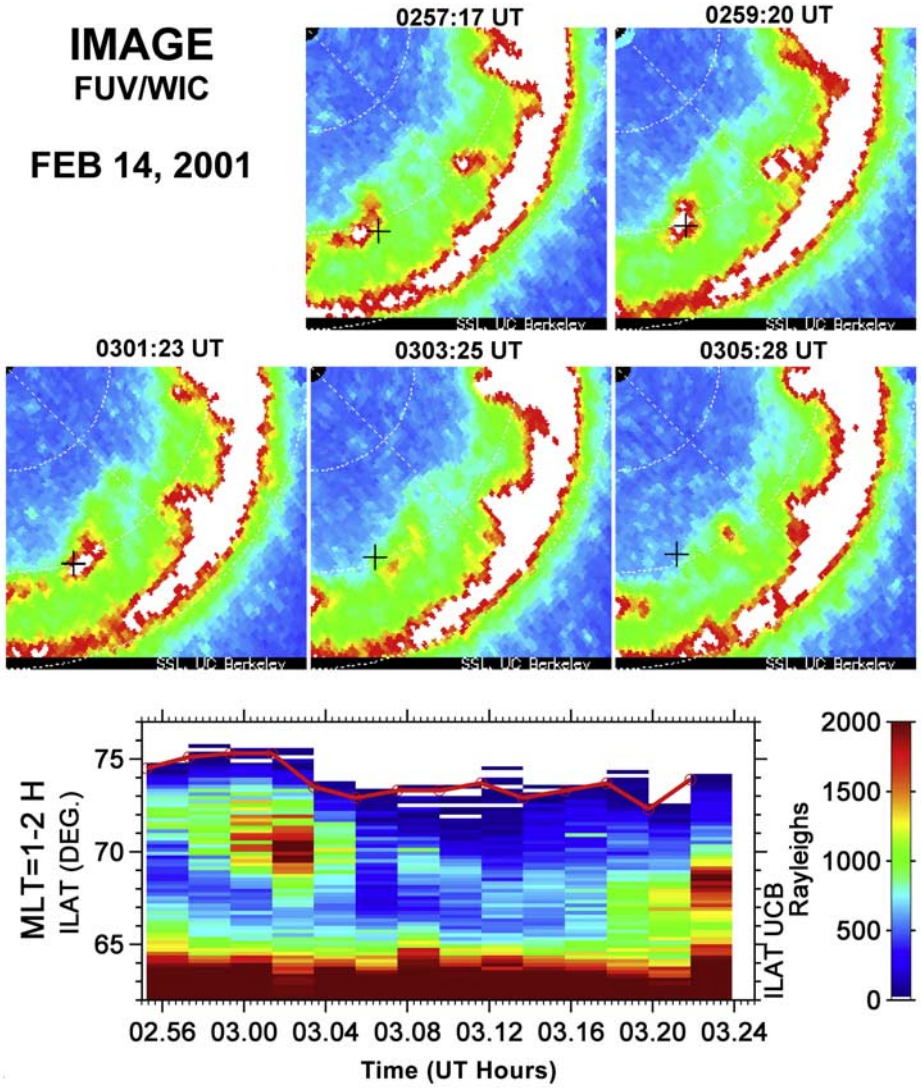

Figure 2. (top) Time sequence of individual images of the 0-6H MLT northern auroral sector and (bottom) ILAT-time keogram integrated over the 01–02H MLT sector, taken by the IMAGE/FUV Wideband Imaging Camera (WIC). The magnetic footprint of the Cluster/SC1 track at 120 km is indicated on each image by a black cross. Note that all IMAGE plots (including Cluster's footprint) were mapped using the Tsyganenko T01 model [*Tsyganenko*, 2002a, 2002b], while all CLUSTER magnetic coordinates presented throughout the paper are obtained through the T89-KP = 2 model [*Tsyganenko*, 1989]. Differences in ILAT are on the order of 1.5°.

(top) and indicates that during this event the prevailing magnetic activity was moderate ($K_P = -4$). Ground-based magnetograms at stations located in the same local time sector (Iqaluit, Leirvogur, and Godhavn) showed the recovery phase of a small, localized substorm (H-component <300 nT) coincident with the period of Cluster observations. For the time interval 0230–0330 UT, Figure 1 (second panel) also shows the three components of the IMF monitored by ACE, lagging by a propagation delay of 34 min. This time interval was characterized by a mainly southward-directed

Figure 1. Interplanetary and ground-based conditions during the 14 February 2001 event. From top to bottom: (a) provisional AE index from 00.00 to 12.00 UT on 14 February 2001 provided by the World Data Center for Geomagnetism, Kyoto (http://swdcwww.kugi.kyoto-u.ac.jp/index.html); (b) GSM components of the Interplanetary Magnetic Field measured by ACE/MFI from 02.30 to 03.30 UT (a propagation time of 34 min has been applied for solar wind to propagate from ACE to Cluster); (c) high-latitude ionospheric convection pattern observed by the SuperDARN radar network between 0300 and 0302 UT. The plotted velocity vectors derived from available SuperDARN radar data are superimposed on the fitting convection model described by *Ruohoniemi and Baker* [1998]. Cluster footprint/motion at 0300 UT is indicated by a yellow dot/arrow (southwest Greenland).

IMF (IMF-$B_z \sim -2/-4$ nT), with short positive excursions of IMF-B_z between 0249 and 0256 UT, i.e., just a few minutes before the interval of interest. For this time period, the solar wind dynamic pressure (not shown) was low ($\sim$2 nPa) and did not show any significant fluctuations.

[13] During this Cluster event (0300–0315 UT), high-latitude plasma convection in the northern ionosphere was continuously monitored by SuperDARN radars. The polar cap global convection pattern for the 2-min radar scan starting at 0300 UT is presented in the bottom panel of Figure 1; the footprint of Cluster at 0300 UT is indicated by a yellow dot. The radar data are best fitted by the typical skewed two-cell pattern for IMF-$B_z < 0$, $-B_y > 0$, even if the morning side radar coverage is relatively poor, which prevents derivation of the full morning cell. Nevertheless, the vortex observed at the ionospheric Cluster footprint at that time interval is particularly interesting. Poleward along Cluster's track, the convection pattern exhibits a postmidnight flow vortex that turns from westward to poleward/eastward.

[14] The IMAGE satellite is in a highly elliptical orbit of 1000–45600 km altitude. The Far Ultraviolet Imager (FUV) experiment on board the IMAGE satellite is composed of three different instruments: the Wideband Imaging Camera (WIC) and two Spectrographic Imagers (SI12 and SI13). They simultaneously observe the global aurora with snapshots of 5–10 s during every 2 min spin period [*Mende et al.*, 2000; *Frey et al.*, 2001, 2003]. Figure 2 (top rows) shows a time sequence of IMAGE/WIC global auroral images of the 0–6H MLT nightside northern auroral sector. This instrument is sensitive to spectral emissions excited by both protons and electrons but, since SI12 did not observe proton emissions, the aurora is likely produced by energetic electron precipitation. The footprint of the Cluster SC1 spacecraft is indicated by a black cross and is located near or within a small active arc in the poleward oval of the double auroral oval, which is a typical recovery phase signature [*Elphinstone et al.*, 1995]. The first image, at 0257:17 UT, shows a weak auroral emission westward of the Cluster SC1 track. A brightening enhancement starts at 0259:20 UT, and the arc moves westward and is crossed by SC1. The third image (at 0301:23 UT) shows a very significant brightening at the same latitude as the spacecraft and confined to a $\sim$1H MLT longitudinal extent eastward of SC1. The subsequent image at 0303:25 UT indicates a further decrease in the local arc emissions, although the auroral oval as a whole maintains the same intensity. The last image, taken at 0305:28 UT, indicates that SC1 is leaving this auroral oval. The same pattern is observed by the SI-13 instrument (not shown), which is more sensitive to low energy electrons. SI12 images (not shown) reveal that ion precipitation near the SC1 track makes no detectable contribution to UV emissions.

[15] The WIC ILAT-time intensity keogram, integrated over the 01–02H MLT sector crossed by SC1, is shown in the bottom panel of Figure 2. It confirms the presence of this localized bright form and allows the identification of the poleward edge of the poleward oval, defined by the dropout to $\sim$0 of the UV intensity. This polar cap boundary remains remarkably stable all along the interval of interest 0303–0318 UT, and is located at 73.2 ± 0.3° ILAT, in IMAGE coordinates.

4. Cluster Observations on 14 February 2001

4.1. Overview of SC1, SC3, and SC4 Data

[16] Figure 3 shows the SC1 (top) and SC3 data (bottom) obtained on 14 February 2001, between 0259 UT and 0318 UT. In analyzing the similarities and differences in the SC1 and SC3 data it is important to keep in mind that both spacecraft were moving poleward and were separated by $\sim$555 km at 0300 UT or, equivalently, by 0.41° of invariant latitude (ILAT) or $\sim$100 s in time; at 0316 UT the separation remained relatively unchanged, $\sim$505 km ($\sim$0.44° ILAT).

[17] For each spacecraft, from bottom to top, are plotted the high-resolution, omnidirectional energy-time spectrograms of the ion energy flux between 4 keV and $\sim$32 keV (panels a1 & a3), the spectrogram of upflowing ions in the 150°–180° pitch angle (PA) range (panels b1 & b3), and the PA distribution for ions from $\sim$0.4 up to $\sim$28 keV (panels c1 & c3). The next panels display the PEACE electron data, showing spectrograms of downgoing electrons in the 0–37° pitch angle range (panels d1 & d3) and the PA distribution for electrons between $\sim$0.9 and $\sim$1.4 keV (panels e1 & e3). Panels f1, g1, f3, and g3 give the V_z and V_y convection velocity components (in GSE coordinates) provided by the EFW instrument. Finally, the three components of the magnetic field are plotted in h1 & h3. Approaching from the CPS, SC1 and SC3 moved along the same MLT, $\sim$1.30–1.40H MLT, and crossed the polar cap boundary at $\sim$0319:00 UT ($\sim$76.55°) and $\sim$0319:20 UT ($\sim$76.29°), respectively, i.e., outside the timescale of Figure 3. A precise multispacecraft identification of the polar cap boundary from electron data will presented in section 4.3.

[18] Panels a1 (SC1) and a3 (SC3) clearly show the detection of multiple energy-dispersed ion signatures, the first fundamental observational result of this study. A series of energy-time dispersions is evident in the high-resolution SC1 spectrogram from 0304 UT ($\sim$73° ILAT) to 0314 UT ($\sim$75.3° ILAT), and is characterized by various energy-time (or latitude) slopes. Three successive energy-dispersed signatures can easily be discerned (labeled E1 to E3) covering a variable energy range of $\sim$15–3 keV for E1 and $\sim$20–10 keV, i.e., shifted toward higher energies, for E2 and E3. One or two additional dispersed features (such as E4) are also detected between 0312 and 0314 UT, but VDIS structures typical of the PSBL [*Bosqued et al.*, 1993] are not seen in this pass. The detailed pattern encountered by SC3 looks similar, but all SC3 observations are shifted in time. This shift appears to be less than 100 s, and more on the order of 40–80 s, but is nevertheless significant (for instance, see the beginning and end of structures E1 and E2).

[19] The second fundamental result is revealed by the three-dimensional ion spectrograms of upgoing, field-aligned ions (UFIs), in the pitch angle range 150°–180° (panels b1 and b3) and the associated pitch angle-time distributions for ions from $\sim$0.4 to $\sim$28 keV (panels c1 and c3). Between $\sim$0300 UT (71.98° ILAT) and $\sim$0304 UT (72.95° ILAT), SC1/CIS-2 detected the presence of a very intense, highly collimated upward flowing ion flux, with a broad peak energy, ranging from $\leq$1 to $\sim$10 keV, or even

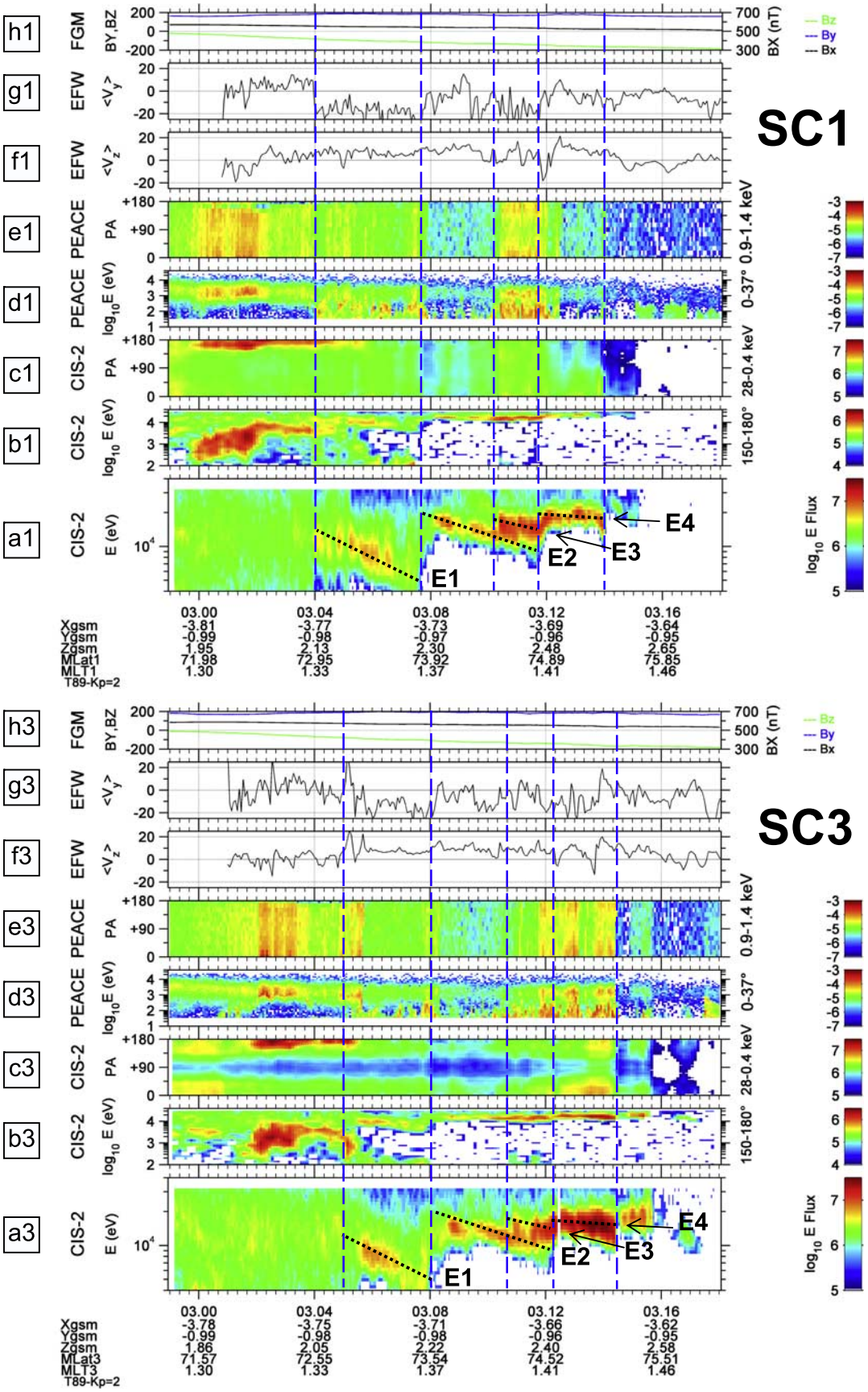
h1
FGM
BY,BZ
BX (nT)
Bz
By
Bx
SC1
g1
EFW
<Vy>
f1
EFW
<Vz>
e1
PEACE
PA
0.9-1.4 keV
d1
PEACE
log10E (eV)
0-37°
c1
CIS-2
PA
28-0.4 keV
b1
CIS-2
log10 E (eV)
150-180°
a1
CIS-2
E (eV)
log10 E Flux
E1
E2
E3
E4
Xgsm -3.81 -3.77 -3.73 -3.69 -3.64
Ygsm -0.99 -0.98 -0.97 -0.96 -0.95
Zgsm 1.95 2.13 2.30 2.48 2.65
MLat1 71.98 72.95 73.92 74.89 75.85
MLT1 1.30 1.33 1.37 1.41 1.46
T89-Kp=2
h3
g3
f3
e3
d3
c3
b3
a3
SC3
Xgsm -3.78 -3.75 -3.71 -3.66 -3.62
Ygsm -0.99 -0.98 -0.98 -0.96 -0.95
Zgsm 1.86 2.05 2.22 2.40 2.58
MLat3 71.57 72.55 73.54 74.52 75.51
MLT3 1.30 1.33 1.37 1.41 1.46
T89-Kp=2

Figure 3

higher in the center (~0302 UT, ~72.4° ILAT) of the ion inverted-V structure. The pitch angle distribution (panel c1) and SC1 ion distribution functions presented in section 4.2 confirm that the ion flux was highly collimated. It can be stated that SC1 was crossing the top of the auroral acceleration region, and ionospheric ions were accelerated up to 8 keV/e or more, presumably by a parallel electric field distributed below the spacecraft. Again, the SC3 observations were similar, and again they were shifted in time by ~100 s. The field-aligned upflowing ions (UFIs) were observed by SC3 during the interval 0301:50 (72.02° ILAT)–0305:20 UT (73.0° ILAT, b3). The observed time shift simply indicates that the upgoing ion flow was continuous (but varying in energy and intensity) for at least 5 min after 0300 UT, in a narrow region of ~1° ILAT extent (from ~72° to ~73° ILAT).

[20] The most remarkable finding provided by the SC1 electron spectrogram (d1) and pitch angle distribution (panel e1) is the presence of an intense inverted-V signature centered on ~0301:45 UT, characterized by an excess of electrons around 1.1–1.2 keV (or $V_{\|}$ ~2.10^4 km/s). The electron distribution function will be analyzed in the next section 4.2 and will show that a field-aligned component is superposed onto a more isotropic background. The same electron inverted-V was detected by SC3/PEACE, centered on 0302:30 UT (Figure 3d3 and 3e3). It can be stated that a nonnegligible part of the parallel potential drop also extended above the spacecraft's altitude, so that the already-accelerated ionospheric H^+ ions observed by SC1 and SC3 probably left the ionosphere after an additional acceleration of ~1–2 keV. The upward flowing ion/downward flowing electron acceleration region was relatively narrow in latitude, ~0.5–1° ILAT, i.e., similar to inverted-V structures observed at lower altitudes [*Bosqued et al.*, 1986b].

[21] The next panels f1-g1 (SC1) and f3-g3 (SC3) in Figure 3 give the V_z and V_y drift components, deduced from the electric field measured by the EFW instruments. The local **B** was directed nearly along $+X_{gse}$ (see h1), therefore V_z gives the poleward component of the convection. Again, details such as local and short-lived increases or spikes in V_z, detected between 0310–0312 UT by SC1, were shifted by exactly 100 s in SC3 observations, i.e., at the same latitude. However, the most noticeable point is that the convection was predominantly poleward-downward during the entire interval of energy-dispersed structures, with $\langle V_z \rangle \sim$ 5–6 km/s, and $\langle V_y \rangle \sim -10$ km/s, from 0304 to 0312 UT, i.e., northward of the localized region of parallel acceleration. Thus the flow direction is in agreement with the SuperDARN detection of a localized vortex. *Kullen et al.* [2008] have recently shown that the plasma flows measured in the ionosphere are a good approximation for the global plasma convection in the magnetosphere, even in regions of strong, field-aligned parallel E fields.

[22] During the 14 February 2001 northern pass, the CIS-1 instruments on Cluster/SC1 and SC3 were running in specific modes that did not allow determination of the local ion composition. Fortunately, the SC4/CIS1 instrument was set up in the suprathermal mode (CIS2 was off). Ion composition data for the 0300–0320 UT time interval are presented in five panels (a–e) in Figure 4, while the EFW dawn-to-dusk E_y component of the local electric field is plotted in panel (f). SC4 followed close behind SC3 in the same orbit, separated by ~3 min in time (and 0.72° ILAT). The longitudinal separation in Y_{gse} between SC4 and (SC1–SC3) was very small, ≤100 km. The most impressive result revealed by the H^+ (panel a) and O^+ (panel c) spectrograms is that the upflowing ion beam region was again crossed, this time between ~0303:20 UT (~71.67° ILAT) and 0308 UT (~72.81° ILAT), i.e., in a region located practically at the same latitude as that of the upflowing ion region observed ~3–8 min before by the leading spacecraft, SC1 and SC3. Moreover, panels (b) and (d) indicate that the upflowing ion beam was remarkably field-aligned and composed of a mixture of 3 mass species, H^+, O^+, and traces of He^+ (not shown). The >100 eV H^+ density was (~0.1–0.2 cm^{-3}), similar to densities recorded in the same region by SC1 and SC3. The O^+ density peaked near 0.05 cm^{-3} and the $n(O^+)/n(H^+)$ density ratio varied between 10 and 50% (panel e), while the $n(He^+)/n(H^+)$ ratio (not shown) was of the order of a few per cent. The O^+ beam appeared to be more energetic than the H^+ beam. Poleward of the ionospheric UFIs, an energetic (E > 6 keV) and isotropic H^+ population was observed up to the polar cap boundary crossed at ~0318 UT (~75.25° ILAT); the very poor time and energy resolution of the SC4/CIS1 instrument during this pass prevents the observation of embedded energy-dispersed multiple structures. Nevertheless, three to four structures can be inferred between ~0308 and ~0317 UT. Finally, the top panel (f) displays the E_y electric field measured by the SC4/EFW instrument. E_y stayed negative for the entire 0306–0318 UT interval and, as the local magnetic field was oriented practically along the $+X_{gse}$ direction, the **E** × **B** convection again pointed in the poleward +Z direction. Thus the SC4 data confirm the SC1 and SC3 observations, specifically the presence of (1) a localized region of ionospheric outflowing ions, but

Figure 3. Cluster CIS-2, PEACE, and EFW data from spacecraft (top) SC1 and (bottom) SC3, for the time interval 0259–0318 UT on 14 February 2001. For each spacecraft (SC1, index $i = 1$; SC3, $i = 3$) and from bottom to top: (a_i) CIS-2 high-resolution one-dimensional energy-time spectrogram (integrated over 4πsr.). Energy scale ranges from 4 to 40 keV; (b_i) CIS-2 energy-time spectrogram for upflowing ions (pitch angle range, 150–180°). Energy scale from 0.1 to 40 keV: (c_i) CIS-2 pitch angle (PA) distribution for ions from ~0.4 to ~2 keV; (d_i) PEACE/HEEA energy-time spectrogram for downward moving electrons (pitch angle range, 0–37°); (e_i) PEACE/HEEA pitch angle (PA) distribution for electrons from ~0.9 to ~1.4 keV; (f_i, g_i) EFW-V_z and V_y (averaged) GSE components of the local **E** × **B** drift (km/s); FGM magnetic field components (nT; B_x right scale, B_y, B_z left scale). Ion flux units are keV/cm^2 s keV (Figure 3a_i), keV/cm^2 sr s keV (Figures 3b_i and 3c_i); electron flux units are ergs/cm^2 s sr eV (Figures 3d_i and e_i). (bottom) GSM spacecraft coordinates (in R_E), invariant latitude ($MLAT_i$) and magnetic local time (MLT_i). The vertical blue guidelines mark the successive energy-dispersed structures E1, E2, E3, and E4.

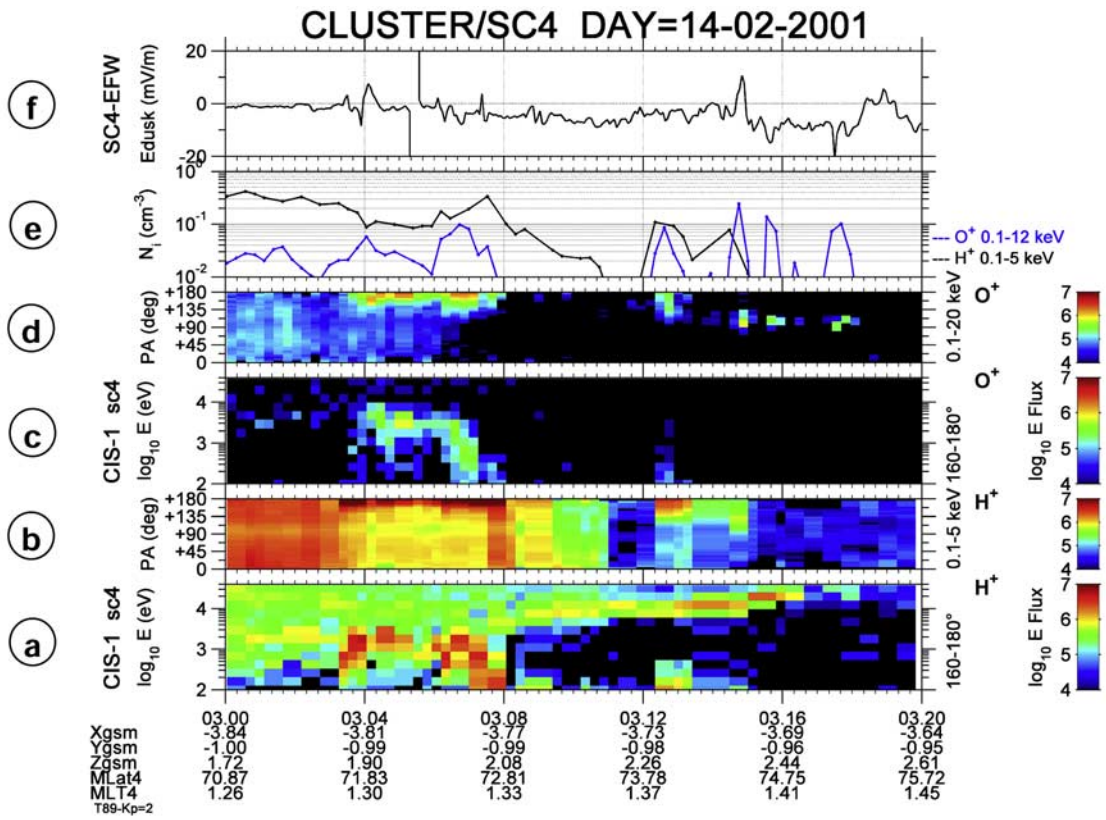

Figure 4. Cluster CIS-1 and EFW data from the spacecraft SC4, for the time interval 0300–0320 UT. From bottom to top: (a) CIS-1 energy-time spectrogram for upflowing H^+ ions (pitch angle range, 160–180°). Energy scale from 0.1 to 40 keV: (b) CIS-1 pitch angle distribution for H^+ ions from ~1 to ~5 keV; (c) CIS-1 energy-time spectrogram for upflowing O^+ ions (pitch angle range, 160–180°); (d) CIS-1 pitch angle distribution for O^+ ions from ~0.1 to ~20 keV; (e) H^+ and O^+ densities, calculated on ground from transmitted distribution functions, in the energy interval of 0.1–5 keV and 0.1–12 keV, respectively.

less energetic and less intense, and (2) a poleward convection component, up to 0318 UT.

4.2. Distribution Functions

[23] Distribution functions recorded during this event are very helpful in characterizing either the acceleration regions or the energy-dispersed structures themselves. Part A (top) of Figure 5 gives a SC1/PEACE electron distribution function taken at 0301:40–48 UT, i.e., during the intense and highly collimated ion outflow; the corresponding SC1/CIS2 ion distribution taken at the same time (0301:45 UT) is given in the left-hand side of Part B. First, concentrating on the ion distribution, it can be seen that the outflowing ion flux peaks at $V_{\|} \sim -900$ km/s (or ~4 keV) and is highly collimated along the magnetic field direction. The electron distribution displays various populations indicative of the presence of a field-aligned electric field located above and below the spacecraft. The velocity space boundaries computed from *Chiu and Schulz* [1978] delineate various regions in the phase space: (1) the $V_{\|} < 0$ atmospheric loss cone is roughly bounded by hyperbola profiles (dashed black curves), computed for a total potential drop from the spacecraft down to the atmosphere of ~4 kV and their asymptotes at ~10° (dotted diagonal lines), (2) a peak in the $+V_{\|}$ direction, confirmed by the differential energy spectrum presented in the right-hand side of part A, bounded by the dashed ellipse at $\sim 2.5 \times 10^4$ km/s (or ~1.8 keV), (3) a significant trapped electron population bounded by the ellipse and hyperbola. All these signatures are characteristic of the existence of a total potential drop of ~6 kV distributed along the magnetic field above and below the spacecraft. The evident widening of the electron loss cone at the lowest velocities results from the presence of the parallel electric field below the spacecraft that accelerates the ionospheric ions up to ~4 keV, while electrons are accelerated downward up to ~1.8–2 keV by the part of the potential drop located above the spacecraft.

[24] The middle and right-hand panels of Figure 5, part B show one set of H^+ and O^+ distributions from SC4/CIS1 taken at 0304:20 UT. It must be noted that the O^+ beam appears to be more energetic than the H^+ beam, and comparison with SC1/CIS2 and SC3/CIS2 distribution functions (without mass selection) indicates that the beams (assumed to be pure H^+ ions) detected by SC1 and SC3 were more energetic, and more intense.

[25] Ion distribution functions typical of SC1 energy-dispersed structures are shown in part C of Figure 5 for three selected times, 0305:58 UT (structure E1), 0308:22 UT (E2), and 0310:34 UT (E3) in the form of the two transverse velocities $V_{\perp}1$ (along $\hat{y}$) and $V_{\perp 2}$ plotted versus parallel velocity $V_{\|}$, in the first two columns, and the two transverse velocities plotted against each other for a $V_{\|} = 0$ cut in the

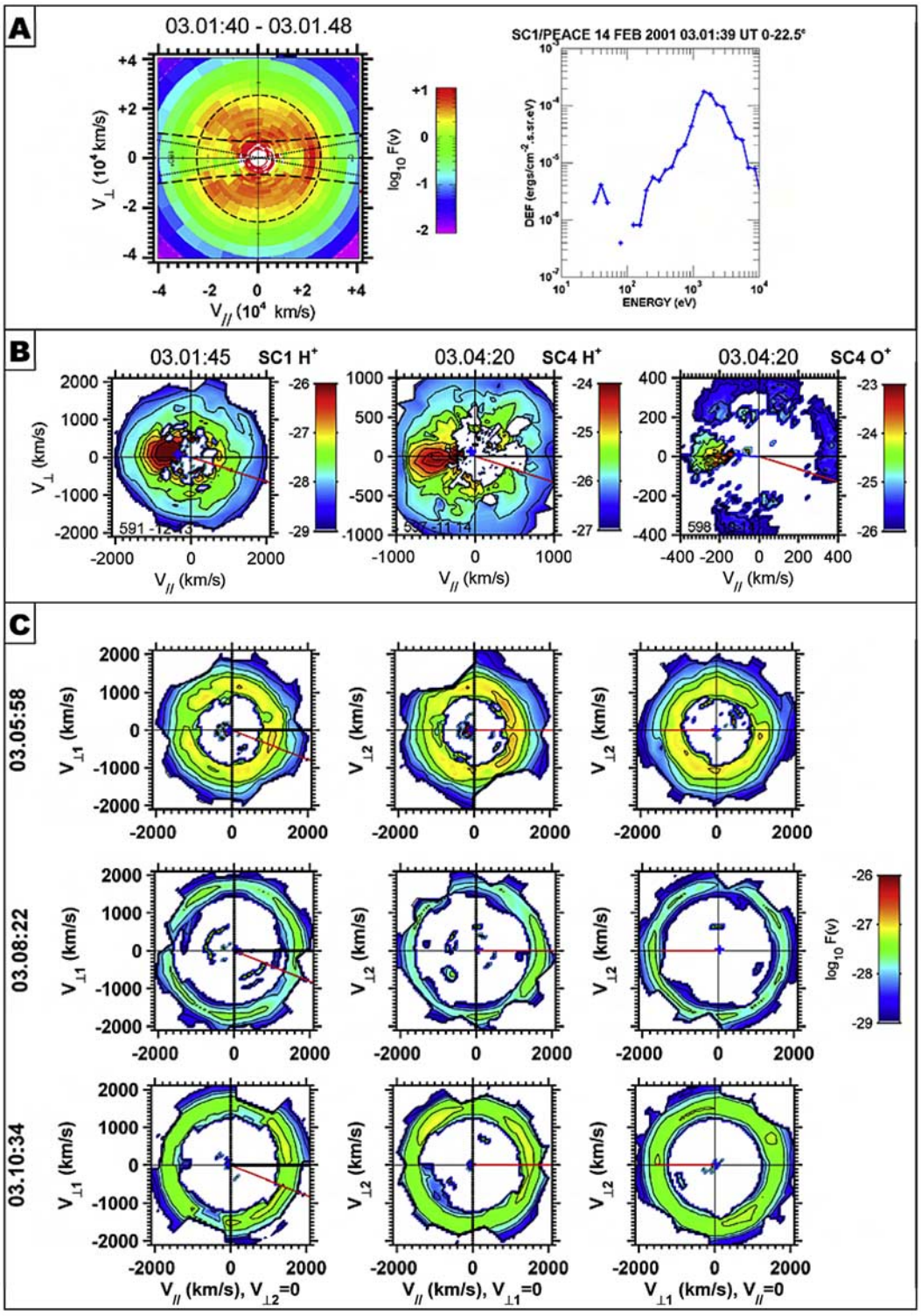

Figure 5. Typical $V_{\|} - V_{\perp}$ cuts of velocity space electron and ion distribution functions. From top to bottom: (a) SC1/PEACE (left) electron distribution taken at 0301:40 UT (integration time, 8s) and (right) differential energy flux spectrum taken at ~0–20° pitch angle. (b, left) SC1/CIS2 ion distributions taken at the same time (integration time, 12 s; all ions assumed to be H^+ ions); (central and right) SC4/CIS1 H^+ and O^+ ion distributions taken at 0304:20 UT (V scales have been adapted). (c) Velocity space contours from the SC1/CIS2 instrument at 0305:58 UT (E1), 0308:22 UT (E2), and 0310:34 UT (E3), whereby the first column shows the first transverse velocity $V_{\perp 1}$ plotted versus parallel velocity $V_{\|}$, the second column shows the second transverse velocity $V_{\perp 2}$ plotted versus parallel velocity $V_{\|}$, and the third column shows the two transverse velocities plotted versus each other for a cut at $V_{\|} = 0$. Positive $V_{\|}$ is along the (downward) **B** direction; and the red vector indicates the X_{gse} direction.

third column. The high-energy ions form a shell distribution, which describes plasma in which all of the ions have about the same drift speed isotropically distributed in all directions of velocity space on a sphere with a radius equal to the shell drift speed. For example, the distribution taken at 0305:58 UT has a shell drift speed of about 1300–1400 km/s (~10 keV for H^+ ions). A small excess in the $V_{\|}$ direction can be noticed on each distribution, while the loss cone is evident on the distribution taken at 0305:58 UT. Ion shell distributions have been observed previously in the near-Earth PSBL by the Polar satellite at low altitudes ≤18,000 km [*Janhunen et al.*, 2003] and by Cluster at ~22,000 km altitude [*Ashour-Abdalla et al.*, 2006]. It is worth noting that ion shell distributions must be observed near the ionosphere each time ions are accelerated along the magnetic field in the equatorial plane where the magnetic field minimizes. Then, the magnetic mirror effect causes a drastic increase in pitch angle of the original beam-like or "kidney bean" distribution. Collimated within a cone of ~10° around a ~15–20 nT magnetic field, the distribution will become a half-shell at Cluster altitude ($|B| \sim 585$ nT at 0306 UT), and a full shell after mirroring below the spacecraft. Aside from a small bump observed in the $V_{\|}$ direction, possibly the signature of an initial field-aligned acceleration in the equatorial plane, these shell distributions do not carry any additional information about acceleration processes.

4.3. Identification of the Polar Cap Boundary

[26] Important, and even decisive as far as the source location could be concerned, is the relative position between the region of energy-dispersed structures, seen to be localized between 73 and ~75° ILAT, and the polar cap boundary. This last boundary is the natural projection of the lobe-PSBL separatrix between open and closed field lines in the downtail region. In order to accurately define the polar cap boundary location, and its possible time/space variations, the low-energy (<30 keV) and high-energy (>30 keV) electron data provided by the PEACE and RAPID instruments, respectively, onboard the four Cluster spacecraft were analyzed in detail. PEACE data are presented in Figure 6 in the form of energy-latitude spectrograms for, top to bottom, the leading SC1 spacecraft, followed by SC3, SC2, and finally SC4. The field-aligned current (FAC) intensity inferred from the magnetic field B_y variations (top) is also plotted for each spacecraft, assuming that current sheets are static and infinite in the y direction. A detailed discussion is beyond the scope of the present paper, but nevertheless it is worth noting that electrons appear as the main carriers of the upward-directed, positive FACs. Concentrating on the electron precipitation and going poleward, various regions may be identified: (1) around 72–72.5° ILAT, the electron inverted-V associated with the accelerated outflowing ions, crossed between 0300 UT (SC1) and 0304 UT (SC2) and slowly shifting equatorward (see also associated FACs); (2) around 73° a new and narrow arc of electrons accelerated to 1–2 keV is detected by SC3, SC2, and SC4 (see also associated FACs); (3) poleward intense electron arcs around 74.5–75°, detected by the four spacecraft; their poleward boundary shifts from 75–75.1° (SC1, SC3) to 74.8° (SC2) and 74.6° ILAT (SC4). This position can be compared to the poleward boundary of UV emissions given by IMAGE, 75° ILAT after intercalibrating IMAGE and Cluster latitudes. Thus from these four electron profiles it can be immediately concluded that the overall electron precipitation pattern (and associated FAC structures) is very steady in time/latitude, and only a slight shift in latitude can be discerned.

[27] We now move to the definition of the polar cap boundary. Poleward of the last electron auroral arc observed around 75° ILAT by the four spacecraft, there is a rather narrow region of diffuse ≤1 keV electron precipitation. *Feldstein and Galperin* [1985] and *Galperin and Feldstein* [1989] proposed that this polar diffuse zone of soft electron precipitation in the ionosphere may be associated with the PSBL in the magnetotail where low-energy electrons are typical [e.g., *Takahashi and Hones*, 1988]. The polar cap boundary can be defined as the dropout of this 1 keV population and is easily identified on Figure 6 at 76.55° (SC1), 76.29° (SC3), 76.30 (SC2), and 76.08° ILAT (SC4). The polar cap boundary defined by the dropout of ~40 keV electrons measured by the RAPID instrument (data not shown) is also reported on Figure 6 and gives similar values: 75.85°, 76.07°, 76.30, and 76.07° ILAT for SC1, SC3, SC2, and SC4, respectively. Thus it can be concluded that the polar cap is unambiguously defined and remarkably steady at ~76° ILAT during the entire event.

[28] As a direct consequence, it can be stated that the main energy-dispersed structures were detected on high-latitude closed field lines between 3° ILAT (E1) and 2° ILAT (E2) from that boundary, i.e., not adjacent to the polar cap boundary, and thus not in the region of ≤1 keV diffuse electron precipitation presumably connected with the PSBL [*Galperin and Feldstein*, 1989] where VDIS are statistically observed [*Bosqued et al.*, 1993].

4.4. Relationship Between Successive Dispersed Structures

[29] The basic issue to be addressed in this paper is identifying the origin of the dispersed ion structures. Experimental evidence (or lack of evidence) for a possible relationship between the successive structures also is of crucial importance. Inverse velocity versus latitude ($1/V - \Lambda$) spectrograms are perhaps the best method to investigate possible time or space relationships and thus infer the location of a common (distant) source. Time-of-flight effects would give linear $1/V$ versus time variations and have been used in the past as evidence of time-of-flight effects on ion bouncing echoes [e.g., *Sauvaud et al.*, 1999], while linear $1/V$ versus latitude profiles are an usual a property of VDIS, whatever their dispersive mechanisms, pure $\mathbf{E} \times \mathbf{B}$ velocity filter effects, or cumulative $\mathbf{E} \times \mathbf{B}$ dispersion and dispersion resulting from a source distributed along the tail, for most common observed B_z profiles [*Zelenyi et al.*, 1990]. Generally, ion traces appear as straight lines and converge toward the computed injection time (or latitude). This property has long been used [see, for instance, *Quinn and McIlwain*, 1979; *Hirahara et al.*, 1996] to infer that the dispersion results from different ion times of flight following a single injection time or location. One of the difficulties arising when using $1/V$ diagrams is that the linear variation (with time or latitude) is only valid under simplified conditions. If an additional acceleration occurs somewhere along the particle journey, however,

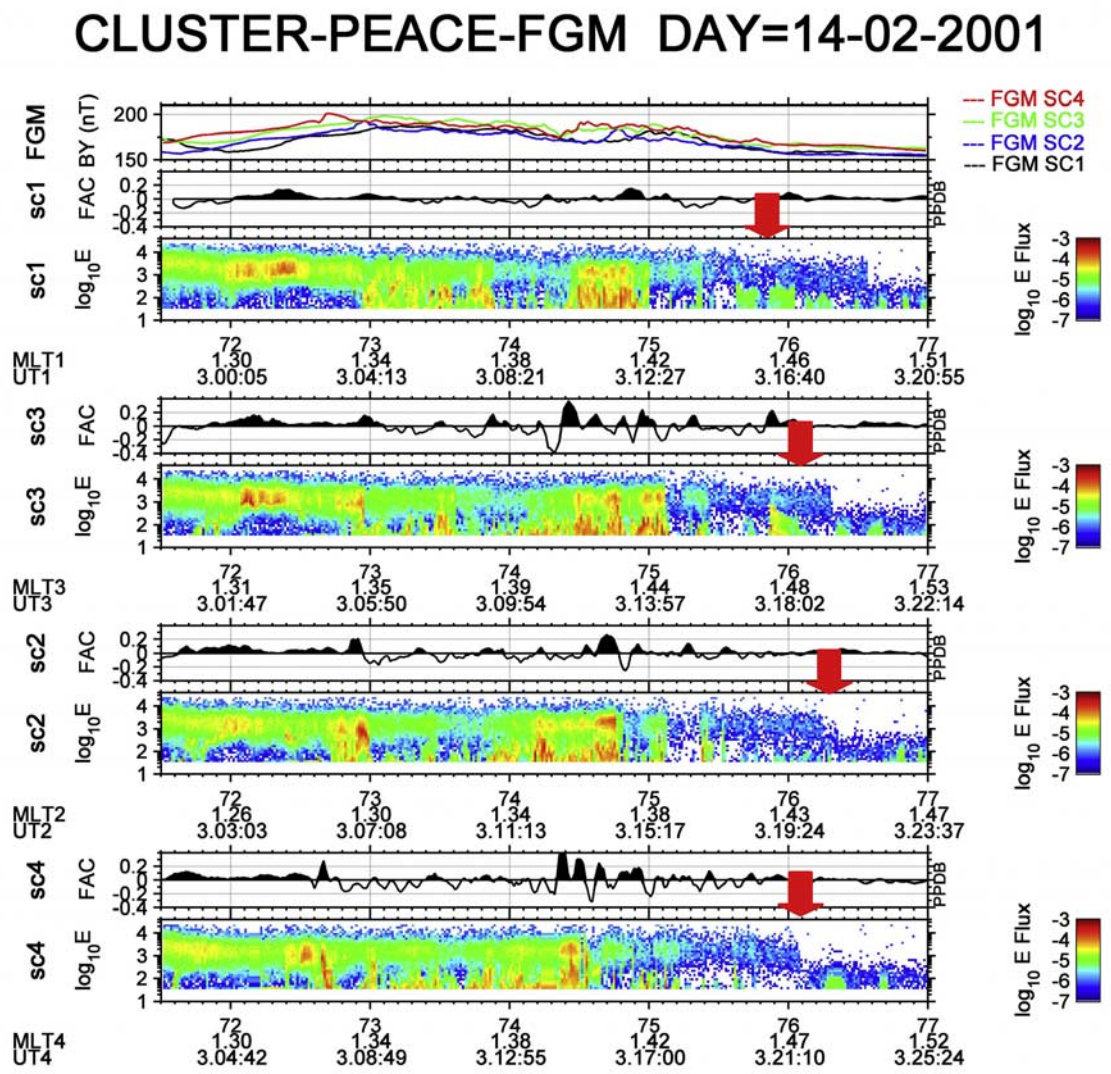

Figure 6. FGM magnetic field and PEACE electron data obtained by the four Cluster spacecraft and plotted versus latitude, from 71.5° to 77° ILAT. The top gives the B_y component of the magnetic field recorded by each spacecraft. For each spacecraft (from SC1, top, to SC4, bottom) are plotted (1) the field-aligned current density (FAC, in μA/m^2) derived from the magnetic field B_y variations (top); upward-directed FACs away from the ionosphere are positive, (2) a color-coded, energy-latitude electron spectrogram from PEACE, giving the differential flux for 0–37° pitch angle range (in ergs/cm^2 str s eV), (3) magnetic coordinates and UT time. For each spacecraft, the red arrow indicates the position of the polar cap boundary defined by the RAPID electron instrument.

additional terms modify the relation and can result in complex, e.g., parabolic, variation [see *Bosqued et al.*, 2006]. $1/V - \Lambda$ inverse velocity (s/R_E) versus latitude SC1 and SC3 spectrograms for the interval 71–76° ILAT are presented in Figures 7b and 7d, together with ordinary spectrograms (panels a and c) already presented in Figure 3, now plotted in linear energy scale and versus latitude. The two dashed parallel blue curves in panels a and c clearly show that the maximum and minimum energies of the structures are linearly increasing in latitude. These same two curves also delimit the energy range of the ionospheric source. We now focus on the $1/V$ spectrograms in panels b and d. In order to avoid uncertainties, or a priori interpretations, and weak associations that result from a visual fit, for each structure the maximum energy flux profile is first computed (solid black profile). We begin by fitting the unaccelerated part of the E1 structure with a straight line (dashed red line) denoting the lowest energy (highest $1/V$) cutoff. This straight line $\Lambda - \Lambda_o = a/V$ intercepts $1/V = 0$ (infinite energy) at $\Lambda = \Lambda_o$. Then the energy flux profile is fitted by a $\Lambda - \Lambda_o = \frac{a}{V}\left(1 + \frac{b}{V}\right)$ parabolic law, where $a \propto V_c.l$, V_c is the poleward convection component and l the travel distance, while b relates to the acceleration increment [see *Bosqued et al.*, 2006]. This fit is given by the solid blue curve, and is tangent to the dashed red curve at $1/V = 0$. Similar parabolic curves are used to fit through structures E2 and E3, and the resulting curves nearly converge to

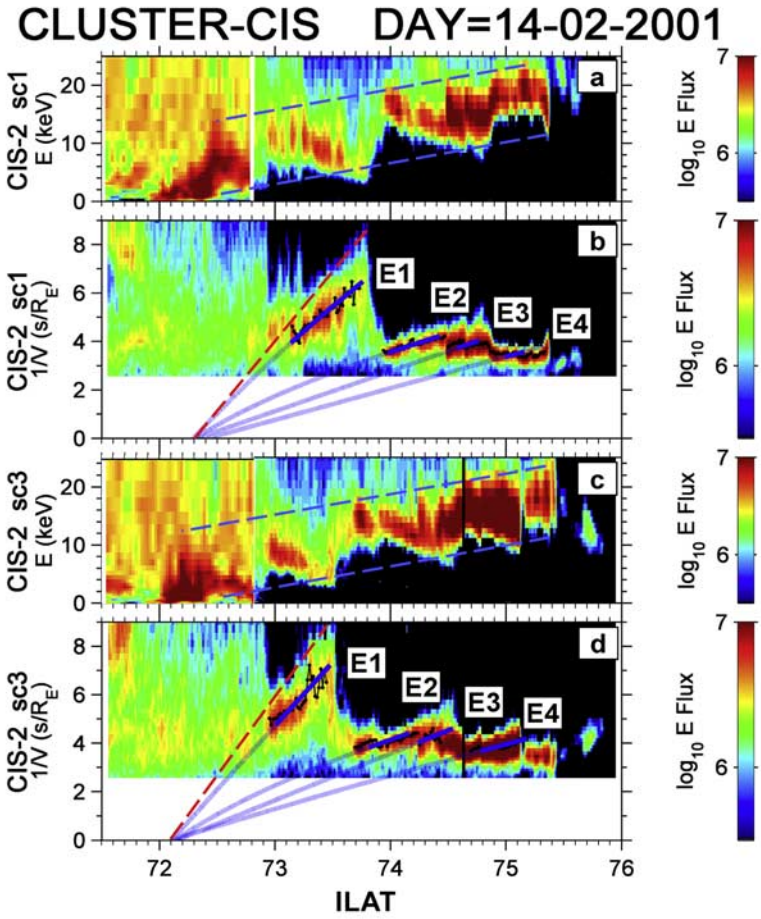

Figure 7. Energy and inverse velocity versus latitude spectrograms for (a, b) SC1 and (c, d) SC3. Energy-latitude spectrograms for SC1 (SC3) are a composite view of Figure 3, b1 (b3) at latitude <72.8° ILAT and a1 (a3) above 72.8° ILAT, and are plotted using a linear scale for energy ranging from 0 to 25 keV. In each energy-latitude panel the two dashed parallel blue lines join the high-energy and low-energy extremities of each substructure. In the 1/V versus latitude panels (b, d), the dashed red line fits the low-energy (high 1/V) cutoff of structure E1, while the maximum energy flux profile of each structure (solid black line) is fitted by the blue parabolic curve converging to ~72.3° (SC1) and ~72.1° ILAT (SC3). See text for more details.

intercept $1/V = 0$ at the same altitude (or latitude range) at or around Λ_0 ~72.3° ILAT. This same result, albeit shifted by 0.2° ILAT (well within the uncertainties in the corresponding SC1 and SC3 latitude mapping), also holds for SC3. These common intercepts suggest that (1) a relationship between the corresponding structures, namely that the structures observed by SC1 and SC3 were initially ejected at the same location, and (2) that the ionospheric outflow present at that latitude range could be the most probable source.

[30] In addition, the dispersion slopes of E1, E2, E3, and E4 get progressively shallower, which implies discrete increases of the $V_c.l$ product [*Bosqued et al.*, 2006]. Assuming the inverse slope for E1 is 1, the calculated inverse slopes of the successive E2, E3, and E4 fits for the SC1(SC3) structures are 1.64(1.61), 3.10(2.74), and 3.91(3.60), respectively, suggesting 1:2:3:4 ratios if the evident large fit uncertainties are taken into account. In other words, this study suggests that the E1, E2, E3, and E4 structures are not at all independent but are constituted by ions ejected from a common initial location and traveling on l distances incrementing in the order 1:2:3:4.

4.5. Summary of Observations

[31] To summarize this experimental section, during a postmidnight pass at an altitude of 4.5–5 R_E above the postmidnight (~1.30–1.40H MLT) northern auroral zone, the series of Cluster spacecraft obtained in less than 15 minutes a nearly instantaneous and similar latitudinal distribution of the plasma populating the midaltitude extension of the CPS-PSBL. Auroral UV images provided by IMAGE/FUV confirm that Cluster was crossing a localized electron arc embedded in the poleward part of the "double" auroral oval, bounded by a very steady polar cap boundary. The basic Cluster observations can be summarized as follows:

[32] 1. Between ~0300 and 0308 UT a stable, continuous, and intense source of ionospheric upflowing H^+ and O^+ suprathermal ions (UFI) was crossed by three Cluster spacecraft; in a narrow ~1–1.5° ILAT region centered on

$\sim$72° ILAT, highly collimated H^+ and O^+ ions were ejected with energies reaching 10 keV or more, which decreased over time to $\sim$2 keV.

[33] 2. This UFI region coincided with an inverted-V electron structure that peaked at 1.5–2 keV energy.

[34] 3. Poleward of the UFI region, the convection drift was observed poleward/dawnward directed by the four spacecraft until 0316 UT.

[35] 4. Three (or more) distinct H^+ energy-dispersed substructures, with energy decreasing from $\sim$30 keV to $\sim$4 keV with time or latitude, were clearly observed poleward of the UFI region by SC1 and SC3 for $\sim$9–10 min. When mapped in latitude, the region of dispersed ramps extended from $\sim$72° to $\sim$75° ILAT, i.e., $\sim$1–4° ILAT equatorward of a very steady polar cap boundary unambiguously identified by <1 keV and <40 keV electrons. Dispersed structures were characterized by (1) similar energy-latitude profiles detected by SC1 and SC3, and (2) an overall increase in average energy from structure E1 to structure E3, and (3) shell distribution functions reminiscent of a field-aligned acceleration at (or near) the equatorial plane of the magnetosphere.

[36] 5. A detailed analysis of the varying dispersion slopes suggest that the ions populating the successive dispersed structures observed by SC1 and SC3 were initially ejected at around the same latitude range centered on 72–72.5° ILAT. Moreover, discrete changes in the successive slopes are indicative of increasing steps in travel distances, in the order 1:2:3:4.

5. Numerical Simulations

[37] The multipoint Cluster data are decisive in settling whether ion energy dispersions result from a temporal or spatial effect. As discussed above, a detailed cross-examination of the SC1, SC3, and SC4 ion data favors a latitudinal coherence in the observation of an upwelling ion source, as well as in the observation of energy-dispersed ramps. Thus the first basic question to be addressed is: what is the origin of the ions observed in the dispersed ion beams? So far, we have identified a potential ionospheric source, now it is critical to gain a thorough understanding of the transport of the upgoing ions ejected from this source. Finally, in case these ions reenter the ionosphere in the same hemisphere, it should be determined whether they can be detected by Cluster as having the expected properties. Furthermore, $\mathbf{E} \times \mathbf{B}$ drift effects must be investigated, as this dispersion would be expected to be poleward, as the convection velocity is observed by Cluster to point poleward throughout the entire interval. This section details our modeling efforts with the ionospheric upwelling region observed by the Cluster spacecraft as our chosen ion source. We will explain our reasoning for discarding the plasma mantle/"stochastic sea" [e.g., *Ashour-Abdalla et al.*, 2005] source in section 6.3 below.

5.1. MHD and LSK Models

[38] Our approach for solving these ambitious problems is to combine the observations with a simulation of the time-dependent transport of ion beams in a representative magnetosphere. To that end, we first quantitatively modeled the overall time-dependent configuration of the magnetosphere by using a global MHD simulation driven by interplanetary (magnetic field, solar wind) parameters. We then used the time-dependent large-scale kinetic (LSK) model developed at UCLA 15 years ago [*Ashour-Abdalla et al.*, 1992] to trace millions of particle trajectories through the resulting electric and magnetic fields. The LSK model has proven to be the best tool for revealing the full complexity of individual ion trajectories and was recently used to successfully interpret Cluster observations from the PSBL [*Ashour-Abdalla et al.*, 2005]. Even in its initial, oversimplified version (time-independent, simple two-dimensional magnetic and electric field models), the LSK technique has given a number of interesting and important new results concerning the physics of particle acceleration in the magnetotail, and has demonstrated the decisive importance of the particles' nonadiabatic behavior [*Ashour-Abdalla et al.*, 1992, 1993, 1995]. This nonadiabaticity results from the value of the parameter κ introduced by *Büchner and Zelenyi* [1986, 1989]: $\kappa = (R_{\min}^{\mathrm{curv}}/\rho_{\max})^{1/2}$, where $R_{\min}^{\mathrm{curv}}$ is the minimum radius of curvature of magnetic field lines at the equator, and $\rho_{\max}$ is the maximum value of the ion Larmor radius near the tail midplane. Ions following field lines connected with the auroral zone typically cross the equatorial plane at distances $\geq$8–10 R_E, and thus exhibit nonadiabatic behavior ($\kappa \leq 2$) and are accelerated by the cross-tail electric field.

[39] For this study we used the global MHD code developed at UCLA [*Raeder et al.*, 1995; *Berchem et al.*, 1998; *El-Alaoui*, 2001] that includes closure of FACs in the ionosphere through the ionospheric potential equation. The possible electrostatic potentials in the conjugate hemisphere (and/or the same hemisphere) were taken into account through this closure. External solar wind conditions (IMF, plasma) monitored by ACE (presented in Figure 1) were used to drive the global MHD simulation, starting on 13 February at 22H UT, to take into account all the effects of past solar wind variations "memorized" by the magnetosphere. The minimum resolution of the simulation grid used in the run presented in this paper was about 0.28 R_E in X, and 0.30 R_E in Y and Z. Results were saved at one minute intervals, and subsequent linear interpolation carried out over time and space produced intermediate values. The next step was provided by the LSK simulations, in which the transport through the magnetotail was investigated by tracing the trajectories of millions of particles launched from the topside ionosphere in time-evolving electric and magnetic fields from the MHD run. Each particle's orbit was integrated by using the full (Lorentz force) equation of motion with a time step small enough to yield an accurate resolution of the orbit details. The time step was 0.002 of the local ion gyroperiod, with an upper limit imposed to prevent too large values in regions with weak magnetic field. This point is particularly crucial, as we anticipate that the ions will drift onto highly stretched field lines and their trajectories will fall in the nonadiabatic regime.

[40] The precise definition of the ionospheric ion source was critical. Cluster data indicate that the energetic ion source detected at $\sim$4.5–5 R_E altitude was present from at least 0301–0307 UT and was concentrated around $\sim$72° ILAT over a narrow region of 1–2° ILAT. On the other hand, the IMAGE/FUV/WIC instrument (Figure 2) gives additional and important information, confirming that a

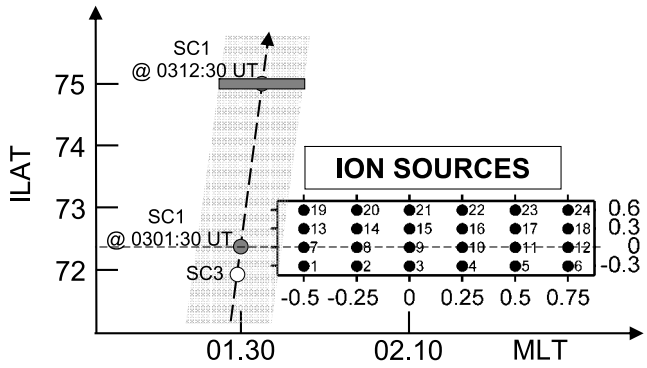

Figure 8. Relative positions of satellite tracks and discrete sources for the LSK code, in ILAT-MLT coordinates. Twenty-four discrete "source" points are placed on a grid, separated by 0.25H MLT × 0.3° ILAT, and constitute the ionospheric source (1.25H MLT × 0.9° ILAT). Source #9, defined as the "central" source, is located at 72.3° ILAT and 0.8H MLT eastward of the SC1 position at 0301:30 UT. The region scanned by the virtual detector (size = 0.4H MLT × 0.15° ILAT, dark gray bar plotted at 0312:30 UT) during its poleward motion is shaded in light gray. The position of SC3 at 0301:30 UT is also indicated.

narrow region of electron precipitation was active for the 0300–0305 UT period; furthermore, its space extent was evaluated to be ~2–3° ILAT × ~1H MLT. Finally, the "ion source" used as input for the LSK code was located in the northern hemisphere at 3.7 R_E altitude (i.e., at the inner boundary of the MHD simulation, near the Cluster altitude at 0301 UT) and was not continuously distributed in this area, but instead was divided into 24 discrete "source" points separated by only 0.3° ILAT × 0.25H MLT (Figure 8). The initial velocity distribution of the H^+ outflow was a drifting Maxwellian with a temperature of 8 keV, an upward field-aligned streaming energy of 8 keV, and was randomly distributed in pitch and phase angle. It is important to note that the full 0–360° range of phase angles must be considered, as phase angle is of prime importance during current sheet interactions and the subsequent nonadiabatic acceleration [*Büchner and Zelenyi*, 1989]. The source distribution function was kept unchanged from 0300 to 0304 UT, and 50,000 particles were launched every 10 seconds during that time interval, from each of 24 source points. Thus the total number of H^+ ions launched in 4 min was approximately $\sim 2.9 \times 10^7$ particles. Each particle was followed until it precipitated into an adaptable "virtual detector," or was lost to the flanks or the tail of the magnetosphere. Furthermore, during the simulation runs, intermediate particle information (location, velocity, time, etc.) was collected by a series of planar virtual detectors located at various places in the system. The spacecraft "virtual CIS detector" was defined as a very narrow slit of surface area moving along the spacecraft orbit. The area of the "virtual CIS detector" was optimized to collect a sufficient number of particles, and was defined as 0.15° ILAT × 0.6H MLT. We note that less than half of the 24 sources contributed ions to this virtual spacecraft detector, and that the "active" sources were concentrated along a rather narrow MLT-ILAT oblique strip ~0.6° ILAT wide.

[41] In order to check whether or not ions were returning along the spacecraft track and being collected by the "detector," a number of preliminary optimization tests were performed by using different locations for the source, relative to the spacecraft track. It is obvious that source location was critical, since returning particles spread out over time and space at various latitudes and longitudes. Figure 8 is a schematic of the optimized relative ILAT-MLT positions of the source points and spacecraft tracks. The source area (24 discrete sources) center point was chosen as 02.10 MLT and 72.30° ILAT (source point #9), i.e., 0.8H MLT eastward of the Cluster SC1 position at 0301:30 UT, since SC1 unambiguously crossed the westward extent of the ion source near that time and latitude. The gray area gives the region scanned by the SC1/virtual detector (dark gray bar plotted at 0312:30 UT) between 0301:30 UT and 0312:30 UT. The position of SC3 at 0301:30 UT is also indicated in Figure 8. Finally, the resulting SC1 and SC3 virtual energy-time (or latitude) spectrograms were constructed to mimic the usual spectrograms from the Cluster/CIS2 detectors. They were obtained by summing in successive energy windows all the returning ions collected by the virtual detector as it moved along the Cluster trajectory.

5.2. MHD Simulation Results

[42] Figure 9 shows the X component of the $\mathbf{E} \times \mathbf{B}$ bulk velocity (left) and the north-south B_z component of the magnetic field (right), displayed as a two-dimensional X-Y map on the surface of maximum plasma pressure which is a very good approximation of the center of the plasma sheet [*Ashour-Abdalla et al.*, 2002; *Peroomian et al.*, 2007]. Throughout the entire 0255–0315 UT time interval the B_z maps indicate that a complex neutral line, defined by a B_z reversal (in black), is present in the near-Earth tail, and is located downtail at $-30\ R_E < X < -24\ R_E$ around midnight. Earthward of this reconnection line, Figure 9 (left) also indicates the presence of two narrow vortex channels of tailward convection centered around $X \sim -15\ R_E$ in the premidnight and postmidnight sectors. We note that field lines passing through Cluster map to the postmidnight channel of tailward flows. Although the magnetosphere changed throughout the 0300–0315 UT interval, the salient features of this configuration plotted at 0304 UT, namely the shape and location of the X line, and the presence of two vortices, remained practically unchanged.

[43] Figure 10a shows a perspective view of the magnetotail configuration at 0304 UT obtained from the MHD simulation, plotted in GSE coordinates. Two field lines are displayed, superimposed over the color-coded background that gives the X component of the $\mathbf{E} \times \mathbf{B}$ bulk flow (red indicates tailward, blue indicates earthward). The black arrows show the direction of the MHD bulk flow velocity. The white field line crosses the Cluster/SC1 position near the Earth, while the black field line intercepts the source region. The results presented in Figure 9 are confirmed by this perspective view, i.e., a vortex-like region is developed in the midnight/dawn sector earthward of the reconnection line, forming a narrow channel of reversed, tailward convection, around $-25\ R_E < X < -8\ R_E$ and $-5\ R_E < Y < -2\ R_E$, embedded in the magnetotail earthward flow. This feature

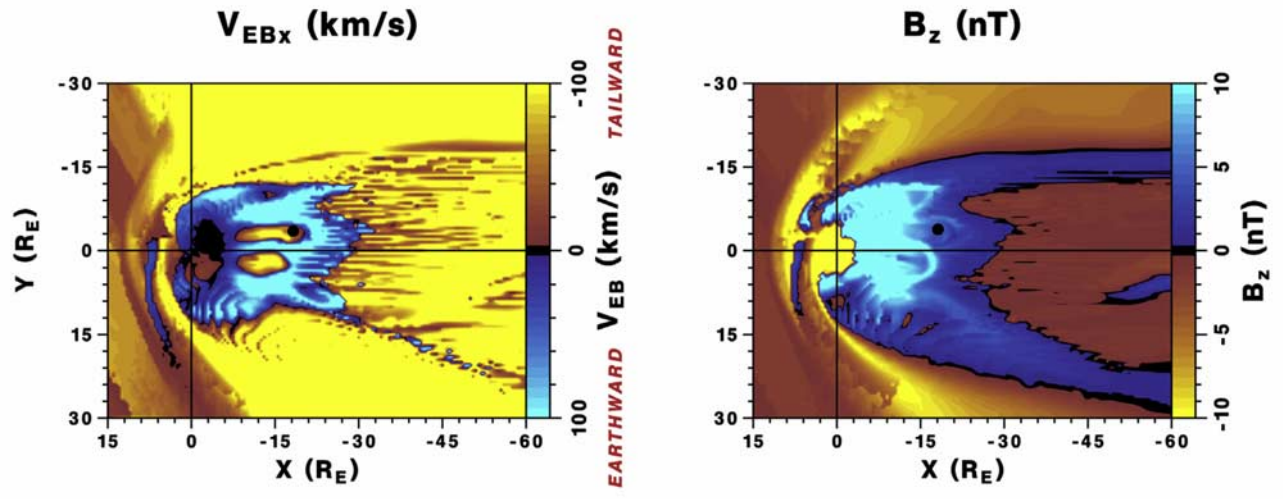

Figure 9. (left) X component of $\mathbf{E} \times \mathbf{B}$ convection velocity and (right) B_z component of the magnetic field in the surface of maximum pressure. The location of the current sheet is determined by computing the surface of maximum pressure in the MHD simulation. The equatorial footprints of Cluster are indicated by a black circle.

is enlarged in Figure 10b, clearly showing the region of tailward MHD flow embedded in a region of tailward convection (red region). This region maps into a poleward convection channel at the Cluster altitude, in excellent agreement with the Cluster data and ground-based observations by SuperDARN (see Figure 1). This is a region of local plasma sheet thinning; such vortices have been already simulated [*Ashour-Abdalla et al.*, 2002; *Walker et al.*, 2006]. This specific topology revealed by the MHD modeling prevails for the overall interval and, as we will see below, significantly affects ion trajectories.

[44] One of the most vital steps in validating our approach is a direct comparison of the MHD simulation results with *in situ* observations, for a sufficiently long period of time. Figure 11 shows the superposition of the MHD simulation data streams over a time series of the magnetic field (top) and drift velocities (bottom) measured at SC1. Comparison of the magnetic field simulated data (black traces) with the SC1 measurements indicates that the simulation is easily reproducing the overall trend and magnitude of the local magnetic field at midaltitude ($\sim$4.5 R_E). The drift velocities measured by the EDI instrument [*Paschmann et al.*, 2001] are also correctly reproduced by the simulation (bottom). The simulation cannot reproduce the large-amplitude spikes observed by SC1 as it crosses the auroral acceleration region around 0301–0302 UT, mainly because of the finite ($\sim$0.28 R_E) grid size of the MHD simulation. This suggests that the grid is too coarse at midaltitudes to resolve the full dynamics of the auroral zone. The possible errors introduced by these rapid variations into our modeling results are discussed in section 6.1. The general trends in the flow data are correctly reproduced, however, including the $V_z > 0$, $V_y < 0$ poleward/eastward drift region observed between 0300 and 0318 UT. There is also good agreement between the simulation results and the observations after 0320 UT, when SC1 reaches the polar cap and the region of antisunward ($V_x < 0$, $V_z < 0$) convection.

5.3. Particle Trajectories and Simulated Spectrograms

[45] Before presenting the virtual spectrograms constructed from the LSK simulation results and their comparison with Cluster measurements, we first elucidate the nomenclature chosen for classifying the different types of ion orbits found in our study. Typically, ions in our LSK simulation experienced multiple neutral sheet crossing during which they were nonadiabatically accelerated in fields varying on short ($\leq$1 min) timescales. Starting from $\sim$4 R_E altitude, i.e., far from the central plasma sheet, ion motion is a combination of gyration, field-aligned motion, and $\mathbf{E} \times \mathbf{B}$ convection. However, upon reaching the vicinity of the current sheet, the motion will change from fast gyromotion around magnetic field lines to slow meandering across the neutral sheet plane. The transition between the two regimes is determined by the parameter of adiabaticity κ (see section 5.2). Therefore instead of using the number of current sheet crossings, we chose instead to classify ion orbits by the number of half (“H”) and/or full (“F”) bouncing periods. For that purpose, we used two virtual plane detectors placed a distance of $|\Delta Z| = 2\ R_E$ on either side of the neutral sheet plane. Ion orbits classified as one half-bounce (“1H0F” for one half-bounce and no full bounce) corresponded to ions interacting with the neutral sheet and then immediately returning to the northern hemisphere (where they originated). One full (“0H1F”) particle bounce corresponded to particles mirroring at an altitude $Z < -2\ R_E$ in the southern hemisphere (and thus not necessarily within the conjugate ionosphere). These 0H1F particles crossed (and interacted with) the current sheet twice before they were detected. Other trajectory families were made up of particles that underwent multiple current sheet interactions made up of combinations of these two basic “H” and “F” trajectory parts, e.g., 1H1F, 0H2F, etc.

[46] The LSK simulation results for SC1 are given in Figure 12, in the form of energy-ILAT spectrograms, which are well-suited to emphasize the latitude dispersion of the collected particles. From top to bottom, the first three panels

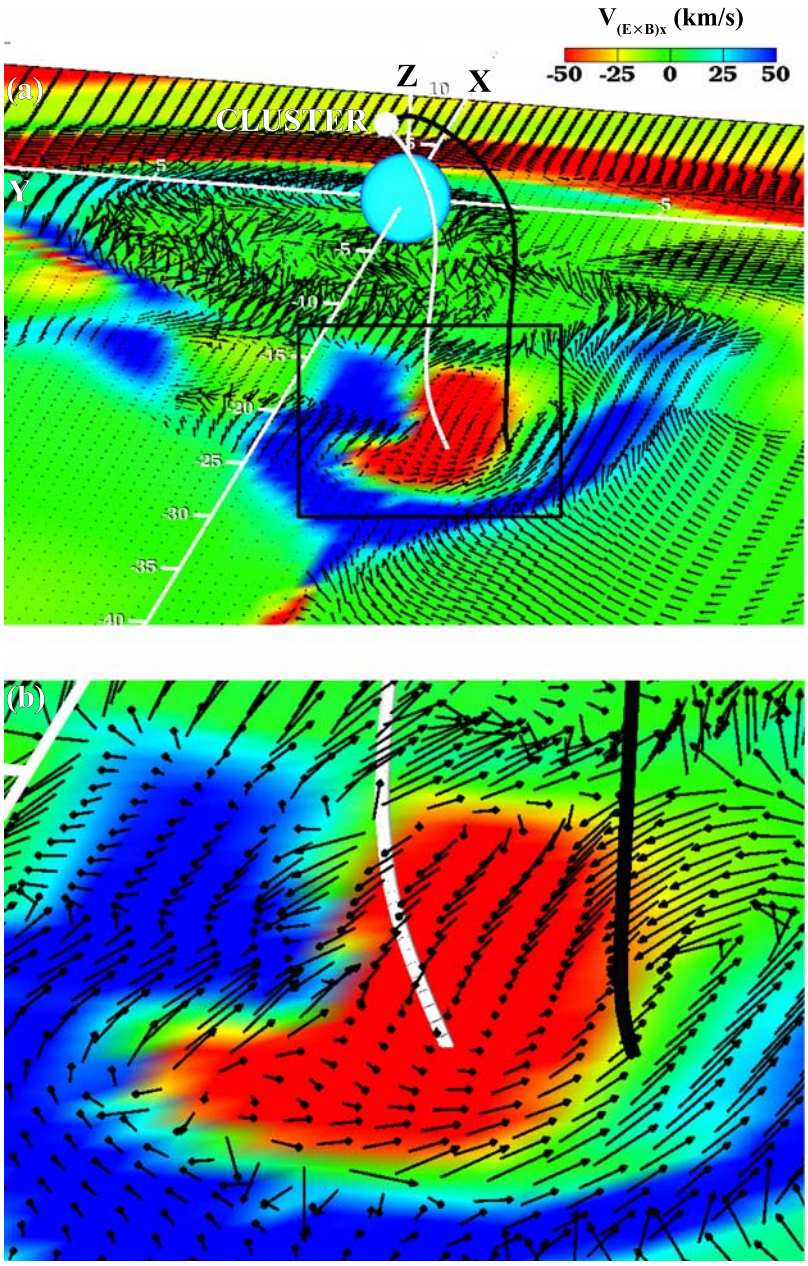

Figure 10. (a) Perspective view of the MHD flow lines (arrows) and color-coded X component of $\mathbf{E} \times \mathbf{B}$ in the GSE equatorial plane at 0304 UT. The white magnetic field line is connected with Cluster/SC1, whereas the black field line maps one ion source located 0.4 R_E dawnward of SC1. (b) An enlargement of the rectangular region in Figure 10a, highlighting the tailward-directed flow in the MHD simulation.

give partial spectrograms, i.e., spectrograms relative to one of the four trajectory categories, 1H0Fa-b, 0H1F, and 1H1F. The fourth panel (entitled *ALL*) gives the full simulated SC1 spectrogram, including all particles, while the bottom panel provides for comparison the experimental spectrogram already plotted in Figure 3. The latitudinal bounds of each experimental E1–E4 energy-dispersed substructure is distinguished by vertical dashed blue lines and fitted by a dotted white line, reproduced for comparison in each particular spectrogram.

[47] Before embarking on a detailed analysis of these trajectories and spectrograms it may be useful to recall the interpretation of these dispersed structures presented in *Bosqued et al.* [2006]. Using a very simplified, analytic model, the first two structures E1 and E2 were correctly modeled and attributed to 1 full bounce (0H1F) and 2 full-bounce (0H2F) particles ejected from the ionospheric source, and slightly accelerated at the equatorial plane.

[48] An examination of the 1H0F spectrogram (Figure 12, top), shows a surprisingly large number of 7–32 keV particles reaching the virtual spacecraft after only one half-bounce. These particles are roughly distributed in two distinct latitude-dispersed substructures, first between 72.50° ILAT (~0302:10 UT) and 73.50–73.80° ILAT (~0306:30 UT), and second between ~73.65°ILAT (~0307 UT) and ~74.8° ILAT (~0312 UT). The second substructure can even be

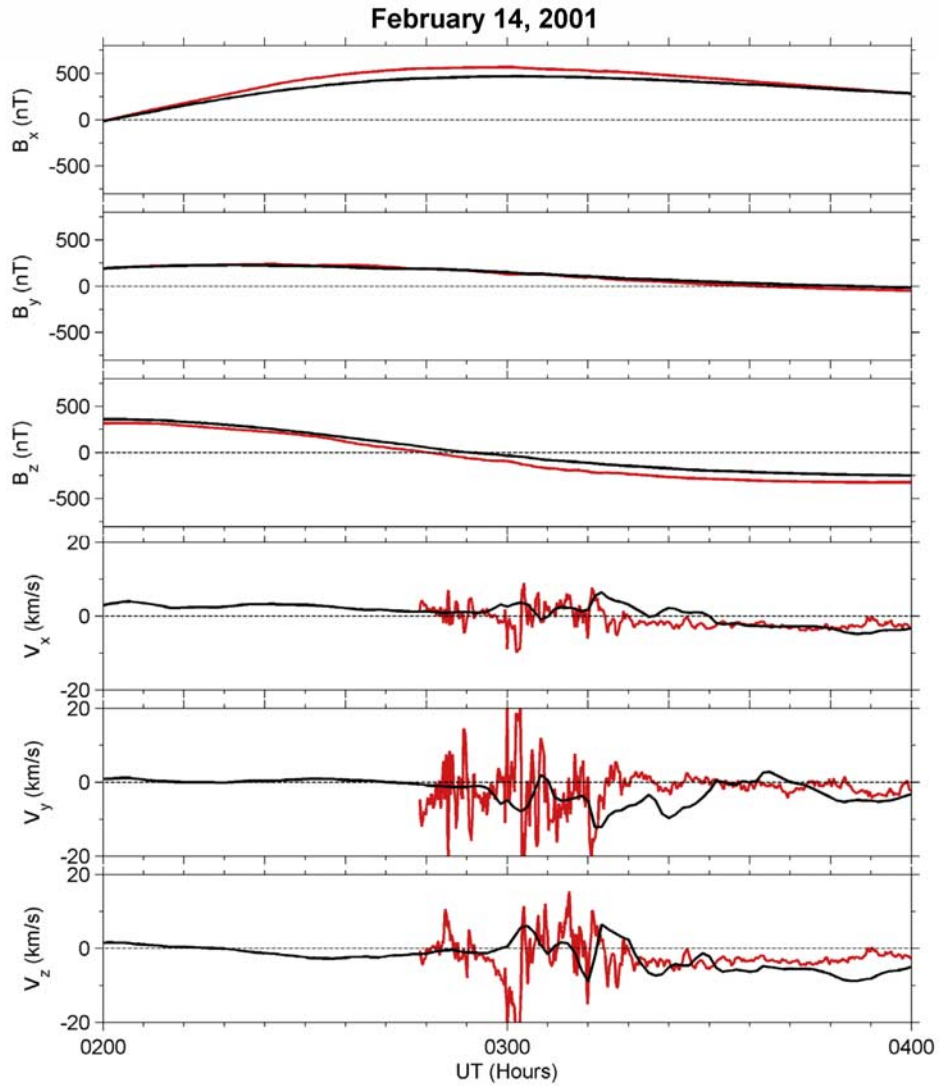

Figure 11. Superposition of 2 hours of simulation data (in black) over a time series of the Cluster/SC1 data (in red). (top) Magnetic field components and (bottom) components of the drift velocity provided by the EDI instrument.

split into two parallel dispersed ramps. When compared to the experimental SC1 spectrogram (bottom, and white dotted fit lines), these two substructures unexpectedly coincide with the E1 and E2 dispersed structures attributed in a previous simplified work [*Bosqued et al.*, 2006, their Figure 3] to particles that were returning to the spacecraft after 1 and 2 full bounces, respectively. This apparent inconsistency will be addressed in the Discussion section below. A detailed examination of individual orbits can be a great aid to understanding the division of the 1H0F family into two subfamilies, 1H0Fa and 1H0Fb. Figure 13 shows four typical trajectories of ions detected by the "virtual" SC1 detector, from the 1H0F, 0H1F, and 1H1F families. The 1H0F category is subdivided in two subcategories 1H0Fa and 1H0Fb, according to the duration of the current sheet interaction. Each ion trajectory is first projected onto the *X*-*Z* and *X*-*Y* planes (top); the time evolution of the ion kinetic energy E (in keV, blue line), and the parameter of adiabaticity κ (red line) along each ion orbit are given in the bottom panel. Details of a typical 1H0Fa family particle trajectory, marked by a black circle labeled (a) in the top panel of Figure 12, are given in the top left-hand panel (a) of Figure 13. Launched from the ionospheric source at 0301:30 UT with an energy of ~4.40 keV, this particle interacts with the neutral sheet at $X \sim -20\ R_E$ and $-2\ R_E < Y < -0.5\ R_E$ around 0303:30 UT, where it first undergoes stochastic acceleration, marked in red along the portion of the trajectory where $\kappa < 2$. The particle follows a "Speiser"-type orbit [*Speiser*, 1965], i.e., oscillates in the current sheet for ~30 s, is energized up to ~11.7 keV, and leaves the neutral sheet after only one half bounce to return to the same hemisphere at ~0305:20 UT, where it is detected by the moving "virtual" SC1 detector.

[49] The principal difference between the 1H0Fa and 1H0Fb subsets of the 1H0F category of half-bouncing particles is the length of the current sheet interaction. The

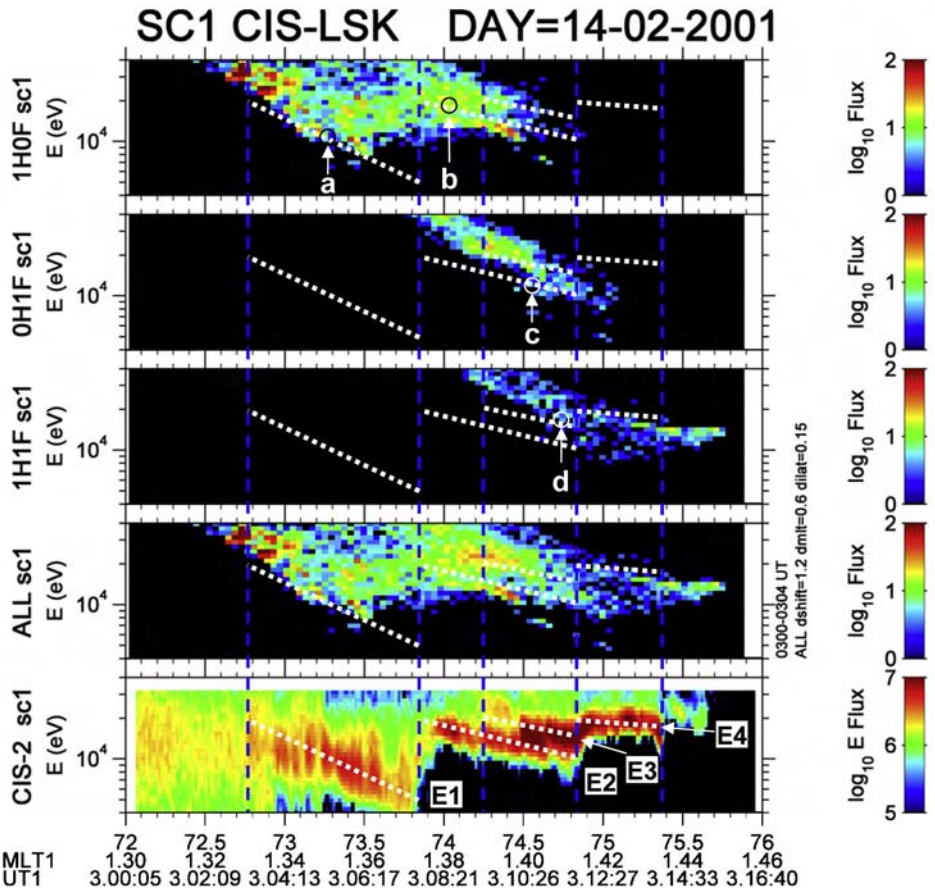

Figure 12. Simulated SC1 energy-latitude spectrograms, compared to the experimental energy-latitude spectrogram (see Figure 3, a_1). From top to bottom are plotted the individual simulated spectrograms (4–40 keV and 72–76° ILAT) corresponding to three trajectory families: 1H0F, 0H1F, and 1H1F. The fourth panel (labeled ALL) integrates all particles, for comparison with the experimental CIS-2 spectrogram (bottom). Indexes a, b, c, and d refer to individual particle trajectories displayed in Figure 13. The vertical light blue guidelines mark the observed energy-dispersed structures E1, E2, E3, and E4. The experimental fitting lines (dotted white) are repeated in each simulated spectrogram. All sources were active during the 0300–0304 UT time period.

trajectory of one particle (with an initial energy of ~8.7 keV) belonging to the second subset of 1H0F particles is given in the top right-hand panel (b) of Figure 13, and is marked (b) in Figure 12. It is evident that this particle, launched at 0301:40 UT, stays trapped for a long time, ~4 minutes, between $X \sim -12\ R_E$ and $X \sim -22\ R_E$. It undergoes successive accelerations and decelerations during two "cucumber"-type orbits [*Büchner and Zelenyi*, 1986, 1989] until it finally gains ~19 keV in energy, is ejected toward the northern hemisphere, and is detected at ~0308:50 UT.

[50] The spectrogram of 0H1F particles, which undergo a full bounce, is given in Figure 12 (second panel from top). A very clear energy-latitude dispersed structure is again evident, located between ~73.9° ILAT (~0308 UT) and ~75.1° ILAT (~0313 UT). This structure appears to be almost superimposed on the most poleward branch of the previously described "1H0Fb" substructure and is in correct agreement with the location and the slope of the E3 structure (white dashed curve). The typical trajectory of a single particle extracted from this "0H1F" full bounce family (white circle labeled c in Figure 12) is also plotted in Figure 13c. The 4.6 keV particle launched at 0303:30 UT first interacts with the neutral sheet at ~0305:15 UT around $X \sim -20$ to $-21\ R_E$, gains energy up to ~7.5 keV, is then ejected toward the conjugate hemisphere, mirror reflects reaches the neutral sheet around 0308:45 UT. During this second interaction the ion gains additional energy and is accelerated up to ~12.1 keV before returning to the northern hemisphere.

[51] The 1H1F family is the last category that significantly contributes to the particle flux detected in the LSK simulation. Once again, a well-formed dispersed structure is simulated, extending somewhat poleward of the 1H0Fb and 0H1F ramps, from 74.2° ILAT (~35 keV, ~0309 UT) to ~75.8° ILAT (~0315:10 UT). One example of a typical trajectory is given in Figure 13d. The H^+ ion starts from the auroral zone at 0302:20 UT with ~14.54 keV energy, first crosses the neutral sheet between 0303:30 and 0305:30 UT at $X \sim -20\ R_E$, where it undergoes complicated stochastic behavior, and finally leaves the current sheet toward the northern hemisphere, where it mirrors at ~0306:30 UT after one half-bounce. The ion is accelerated twice more, at

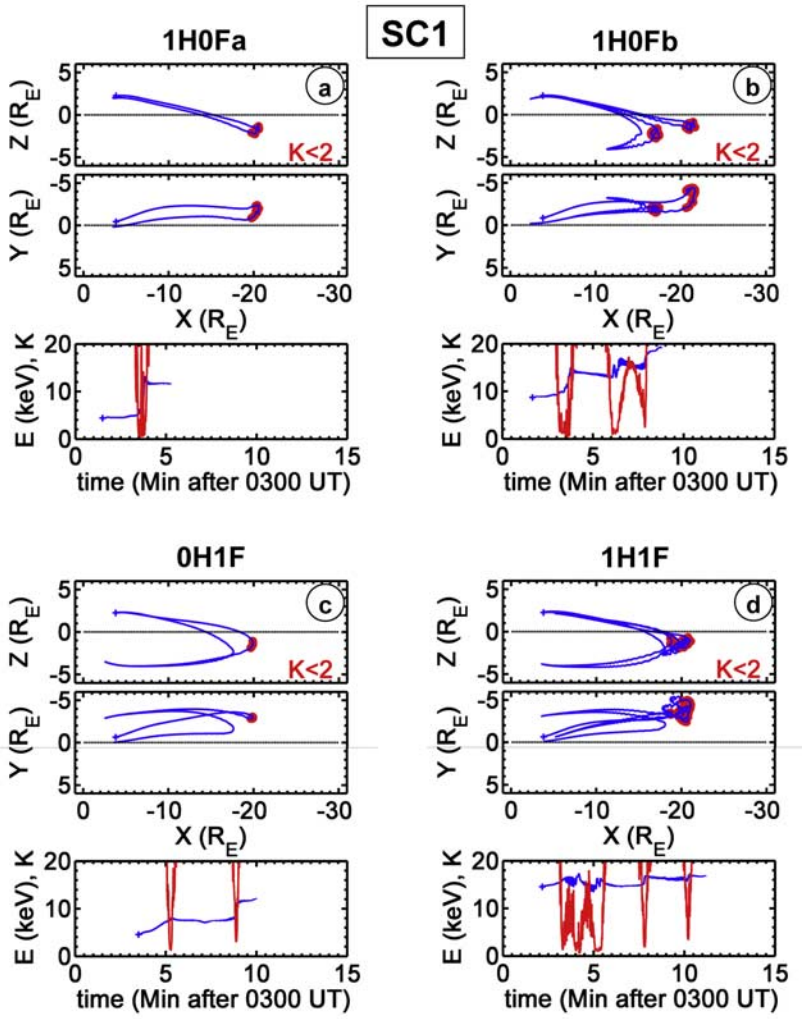

Figure 13. Four typical ion trajectories detected by the virtual SC1 detector: (a) category 1H0Fa (1 half-bounce, 0 full bounce, subset a), (b) category 1H0Fb, (c) category 0H1F, (d) category 1H1F. See text for more details. For each ion trajectory, the three panels show, from top to bottom, the *X-Z* and *Y-Z* projections of the ion trajectory, the ion kinetic energy (keV, blue line) together with the parameter of adiabaticity κ (red line), as a function of time. The portions of the orbits where $\kappa < 2$ are indicated in red.

~0307:45 and 0310:10 UT during the full bounce, and finally returns to the northern hemisphere at ~0311:20 UT (with 16.8 keV energy).

[52] One last comment concerns the time-of-flight and subsequent precipitation. The half-bounce part (1H) of the particles classified within the 1H1F family is highly variable, extending from a short single or double "cucumber" (like the trajectory presented in panel b, classified as a 1H0Fb trajectory) to a nearly full half-bounce (panel d). Therefore many of the particles itemized in the 1H1F family could be just as well classified as 0H2F particles. For this reason, the dispersion in latitude and acceleration can be variable and accounts for the energy-latitude spread observed in the spectrogram between 74.7°ILAT (0311 UT) and 75.35° ILAT (~0314 UT), followed by a clearer structure up to 75.8° ILAT.

[53] The LSK simulation results presented above demonstrate that ions, after being ejected from the ionosphere, follow a great variety of orbits, as a result of partial bounces (mirror points above the Cluster altitude), complex interactions with the current sheet leading to nonadiabatic acceleration, and short ejections in the form of well-known cucumber orbits [*Büchner and Zelenyi*, 1986, 1989]. Their classification into families, defined in the simulations by the number of half-bounce trajectories crossing the $Z = \pm 2\ R_E$ planes, can appear as somewhat arbitrary. Despite this complexity, the LSK simulations plotted in Figure 12 reveal that ions are clearly spread in latitude over 3–4° ILAT, poleward of their ionospheric source. They also unambiguously reveal a structuring in a number of adjacent or overlapping substructures with the correct dispersion, i.e., energy decreasing with increasing latitude. Separate spectrograms are decisive in interpreting the origin of the experimental structures. Thus the first conclusion reached is that the observed substructure E1 coincides in latitude with the simulated substructure composed of 1H0Fa ions alone, i.e., those that undergo only a half-bounce. At this point it is worth noting that this half-bounce echo is, to our

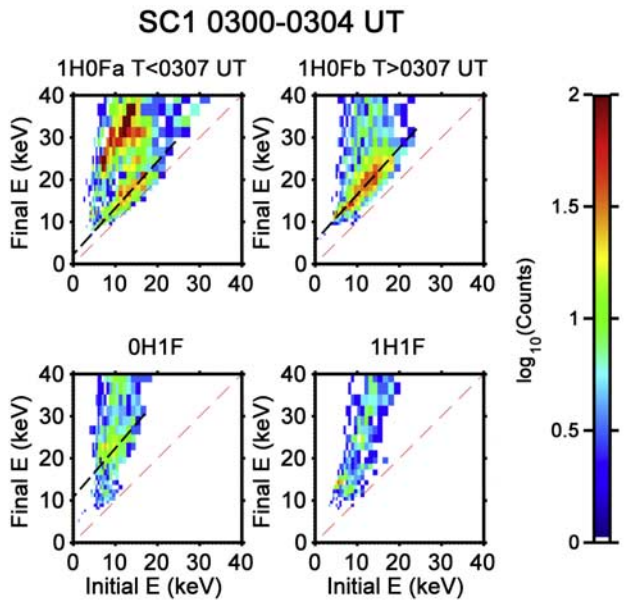

Figure 14. Final energy (keV) versus the initial energy (keV), for each category of trajectories. Particles were ejected from all sources, from 0300 to 0304 UT, and the integrated number of collected particles in one energy bin is color-coded. The dashed black lines indicate the amount of energy gain.

best knowledge, the first seen both in data and simulations. The LSK simulation clearly shows that almost all ions undergo acceleration; the final energy reached in the simulation seems somewhat larger than observed, even though higher energy bursts can be also identified within the experimental structure. Moreover, the lower energy extension of the dispersed structure, down to ~4 keV, is not reliably modeled. Limitations and/or discrepancies between experimental observations and simulations will be discussed in section 6.1.

[54] Interpretation of the second dispersed structure labeled E2 in the data is more complex. After 0310 UT, this E2 structure overlaps with and blends into the more energetic E3 structure (Figure 12, bottom). The simulations are again decisive, because they predict two distinct energy-latitude structures, each associated with a distinct family of bouncing orbits. One can easily associate the E2 structure with the lower-energy branch of the 1H0Fb family, leaving the E3 structure to be composed of full one-bounce 0H1F ions and part of 1H1F ions. This last family of 1½-bouncing ions precipitates in a region that extends up to ~75.7° ILAT in the simulation, but at lower energies and less intense fluxes than the E4 substructure. We have already mentioned that higher order bouncing ions, for example, 2-bounce ions (0H2F in our terminology), were practically absent in the LSK simulations, but part of the 1H1F ions could be considered as belonging to the 0H2F family. Simulations show an additional structure coincident with, but at lower energies than the most poleward structure (not referenced).

[55] The ion trajectories shown in Figure 13 clearly indicate that particles gain variable amounts of energy after multiple half and/or full bounce motions. Figure 14 shows a synthesis of the energy gained by particles during their interaction with the neutral sheet, in regions where the κ parameter falls to ≤ 2, for each of the four families of trajectories. It is notable that the higher the number of interactions with the neutral sheet, the higher the energy gain. For instance, 1H0Fb half-bouncing particles, during their rather complex and lengthy interactions, gain ~5 keV, whereas full bouncing particles gain ~10 keV on average. In reality, owing to the complexity of the interaction, a great dispersion in the acceleration occurs, particularly for the a priori simple 1H0Fa half-bounce trajectories. While the core of this population gains only ~2 keV, larger accelerations can occur. It must be remembered that the motion occurs in time-varying electric and magnetic fields, and that this motion occurs in a region where the electric field is spiky and even reversed (tailward convection), resulting in partial acceleration and/or deceleration. As a result, it is probably unrealistic to use simple considerations to evaluate the anticipated acceleration. For nearly field-aligned particles with initial velocity V_{xi} and equatorial $\kappa < 2$, an approximate expression for their energy increase ΔW during an interaction with the current sheet can be derived as $\Delta W \approx 2mE_y/B_Z(E_y/B_z - V_{xi})$, where E_y is the dawn-dusk electric field across the tail and B_z is the magnetic field normal to the sheet [*Speiser*, 1965, 1968; *Lyons and Speiser*, 1982; *Lyons and Williams*, 1984]. Using the empirical relation given by *Boyle et al.* [1997], the total polar cap potential drop (or the dawn to dusk potential) is approximately $\sim 16.5 + 15.5\ K_P$, or ~67 KV for 14 February 2001 at ~0300 UT, compared to 56 KV, the potential derived from the SuperDARN map presented in Figure 1. If the tail diameter is on the order of 30 R_E, E_y is ~0.3 mV/m on average. If we assume $B_z \sim 1$ nT, very low-energy ions ($V_{xi} \ll E_y/B_z$) will escape ~1 R_E duskward of their first crossing, and gain $\Delta W \approx 2m(E_y/B_Z)^2 \sim 1.8$ keV during the interaction, while 8 keV protons will gain ~5.4 keV and escape ~2.5 R_E duskward.

[56] Thus the energy gain in the LSK simulations is in agreement with the observations and is correctly described by a "Speiser" type duskward drift through the large-scale electric field. Moreover, one of the strongest constraints imposed by data was the linear energy increase observed in latitude (time) from the outflowing source to the first E1, and then from E1 to E2, to E3, and to E4. The simulations correctly reproduce this linear energy stepping from one structure to the next, proportional to the number of accumulated interactions with the current sheet.

[57] Figure 15 compares the results of the LSK simulations with observations from the SC1 and SC3 spacecraft. The top two panels duplicate the bottom two panels of Figure 12 and show SC1 results, while the corresponding panels for SC3 are shown in the bottom two panels of Figure 15. For each spacecraft, the detected E1, E2, E3, and E4 substructures are delimited by light blue vertical dashed lines that extend to the simulation panels to help in identifying the origin of these substructures. Each labeled structure is also highlighted by its linear logE-ILAT fit (white dotted lines). Before discussing the validity of the simulations, two points must again be emphasized: (1) the SC1 and SC3 observations are similar, particularly in that the extent and fitting lines for the main structures, E1-E2-E3 are identical, while structure E4 appears as more intense and

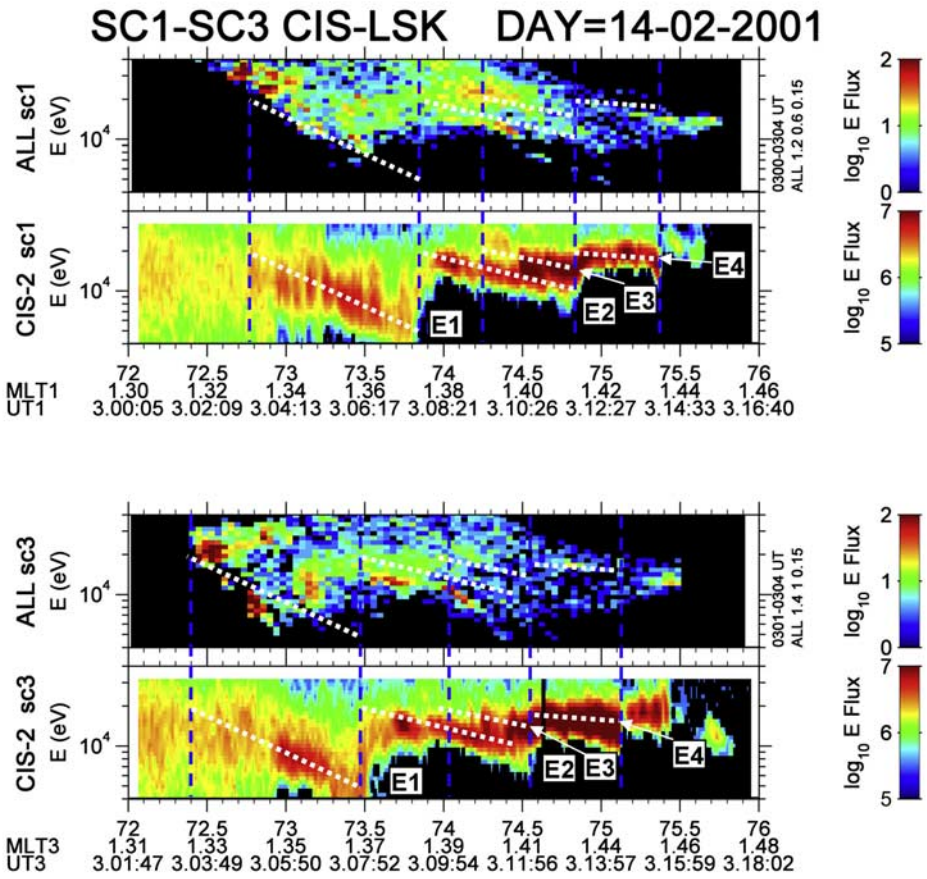

Figure 15. Simulated and experimental SC1 and SC3 energy-latitude spectrograms. Top panels duplicate the bottom part of Figure 12 for SC1. SC3 spectrograms (identical format) are displayed in the bottom two panels.

at a lower energy when detected by SC3, and (2) these observations are not coincident in time (see Figure 3), nor are they exactly coincident in ILAT; when detected by SC3, the structures are shifted equatorward by 0.3–0.4° ILAT.

[58] The details of the comparison between the simulated and observed SC1 structures also hold for the most part for SC3. Once again, the LSK simulations reveal that the E1 structure detected by SC3 is made up exclusively of half-bouncing ions (1H0F). The simulated structure is composed of patchy substructures, not all of which are visible in the data, while the part near the end where <10 keV, detected between 73 and 73.5° ILAT is not correctly reproduced by simulations. We note that the source was switched on at 0301 UT, not at 0300 UT (as in the SC1 simulation), for the SC3 simulations. Switching on the source at 0300 UT would add a large number of 1H0F ions returning to the source latitude, i.e., apparently without any $\mathbf{E} \times \mathbf{B}$ dispersion. This point will be discussed below. Still, for SC3, the major part of the E2 structure corresponds to the lower energy branch of 1H0Fb (half bounces with a long stay in the current sheet and/or additional "cucumber" orbits). The double input from full-bounce (0H1F) and 1H1F particles generate the E3 structure. E4 is more difficult to interpret, although simulations show that a part of the 1H1F family coincides in latitude and energy (but not in flux) with E4. Finally, as for SC1, a last, poleward structure is simulated.

[59] The most impressive result delivered by the LSK simulations comes from the multipoint comparison. In addition, to providing an innovative interpretation of each structure, the MHD+LSK simulation reproduced the exact latitudinal extent of the observations, between ~72.5 and ~75.8° ILAT for SC1, and the shift of 0.3–0.4° ILAT noted between the SC3 and SC1 observations. A detailed examination of the drift maps (not shown) provided by the MHD global simulation demonstrates significant variations on a 1-min scale, in agreement with the data. Cluster measurements in the 0302–0308 UT interval (see Figure 3) indicate that the averaged $\langle V_z \rangle$ poleward component was +5.65 km/s (σ = 3.80 km/s) when first measured by SC1, but decreased to only 4.32 km/s (σ = 6.30 km/s) by the time it was detected by SC3. This difference of ~1.3 km/s will introduce an offset of ~400 km after a 5 min drift between similar structures observed successively by SC1 and SC3, equivalent to ~0.4° ILAT. For instance, the E1-E2 boundary is detected at ~73.85° ILAT by SC1, and at ~73.45° ILAT by SC3. Thus it follows that convection changes are also correctly reproduced by the simulations, and account for the observed ILAT offset between SC1 and SC3 observations. An additional prediction based on the simulations can also

be understood in terms of drift motion. The virtual SC3 detector collected 1H0F particles injected between 0300 and 0301 UT (not included in SC1 simulations presented in Figure 12) at practically the same latitude as the source, i.e., without any poleward drift. Up to ~0305 UT, SC3 effectively detected very small convection, $\langle V_z \rangle \sim 0$ (see Figure 3), but returning particles were not detected. That means the source was not very efficient before 0300-0301 UT, or that it was located westward of the spacecraft location. IMAGE observations presented in Figure 2 confirm that the source was partly west of the spacecraft track.

5.4. Summary of MHD/LSK Simulations

[60] The results of the coupled MHD-LSK simulations can be summarized as follows:

[61] 1. The MHD code predicts the connection of the Cluster stretched field lines with a vortex-like region of tailward/poleward convection, embedded in the earthward-directed flow for more than 10 minutes.

[62] 2. The LSK simulations reveal that ionospheric particles follow various trajectory families that emerge as spatially overlapping but distinct structures, with the correct energy dispersion in latitude (i.e., energy decreasing with increasing latitude). The physics of ion acceleration contributing to most of these structures were unexpected before the simulation runs.

[63] 3. In spite of a number of limitations, the simulated structures can account for the observed energy-latitude dispersed substructures. Time-of-flight effects are present, but largely attenuated.

[64] 4. The LSK simulations show that the active ionospheric source was located ~0.8H MLT eastward of the spacecraft track and was not very efficient before 0300 UT, in agreement with IMAGE observations; the most "active" source is concentrated along a narrow MLT-ILAT strip ~0.6° ILAT wide.

[65] 5. Successive simulated energy-dispersed structures, directly related to an increasing number of current sheet interactions, display an overall increase in energy, in full agreement with the observations.

6. Discussion and Conclusions

[66] In this section, we first discuss the limitations of the MHD+LSK simulation technique and our choice for the launch distribution of ions, followed by an analysis of alternate interpretations for the origin of the structures observed during this event including the early analysis by *Bosqued et al.* [2006], and close with our concluding remarks.

6.1. Simulation Limits

[67] An important point about our MHD + LSK simulation approach concerns the limits of each of these simulation techniques. Since time dependence was of prime importance, the best available global MHD model was used to simulate the **E** and **B** topologies in which particle trajectories were followed. This model was able, among other things, to predict the localized channel of poleward (tailward) convection, which was needed to validate the space dispersion invoked in this paper. In order to keep the LSK simulation results manageable, a rather simple spatial and temporal ion source profile was chosen. Although the source was delineated as closely as possible to the observed source, the initial distribution was simplified, and the energy and flux of upflowing ions were kept constant in time and space. These simplifications invariably influenced the final results presented above.

[68] It was noted in section 5.3 that the final energies reached in the simulation seemed somewhat larger than observed, and that the simulation failed to predict the lower energy part of each structure, and consequently their poleward portion. This discrepancy is directly related with the definition of the initial source. In addition, as noted in section 5.2, the MHD simulation, because of its coarse grid size of ~0.28 R_E at midaltitudes, could not reproduce the rapid variations in **v** (and therefore **E**) as the Cluster spacecraft crossed the auroral zone. The slow variation of electric fields in the MHD simulation may affect the final particle distributions by, for example, producing a more diffuse range of energies, or in failing to reproduce directional changes in the electric field, give ion energies and/or locations that are slightly different than those observed. These shifts do not, however, alter the physics of the ion trajectories nor affect the conclusions of this paper.

[69] The initial distribution was chosen to be a field-aligned drifting Maxwellian centered on 8 keV with a 8 keV temperature. Although somewhat hotter than the observed source (in reality T ~ 5 keV), such a Maxwellian may represent the center of the ionospheric source observed by SC1 at ~0302:10 UT (see Figure 3). However, it is quite evident that the drift energy and temperature drastically decrease on both sides of the inverted-V, e.g., to 5 keV and 3 keV, respectively, around 0301 UT. Decreasing the initial energy would decrease the nonadiabatic energy gain, and therefore the final energy reached; Moreover, after a longer time of flight, the particle would be dispersed to a higher latitude and would be more easily collected by the virtual spacecraft detector.

[70] All 24 ion sources were switched on for only 4 min, from 0300 to 0304 UT. This "illumination" period was determined first from observational arguments (auroral arc detected by IMAGE/WIC), and was later justified by the very low contribution of ions launched before 0300 UT and after 0304 UT. Moreover, the injected flux was kept constant over time and space; this limitation could account for a number of differences or discrepancies observed between observations and simulations. These main differences are (1) the number of collected particles appears low in comparison to the number of ejected particles, (2) distinguishable structures are embedded on background noise, particularly structures related to 1H0F and 1H1F subsets, and (3) the simulated flux for the E3 and E4 structures are well lower than the experimental flux. Because of the nonadiabatic nature of the acceleration mechanism operating during each interaction with the neutral sheet, it is not easy to foresee or predict the consequences of varying the outgoing flux over time and/or space. Two distinct accelerated populations are formed during each interaction, particularly during the first neutral sheet crossing: (1) the coherent population, accelerated on Speiser-type orbits that escape field-aligned and come back immediately to the detector, and (2) the second population, also accelerated but in a randomized way, that is scattered to stay

trapped in the vicinity of the current sheet on more or less short "cucumber-shaped" orbits. The relative intermixing between these two populations varies according to the site of interaction, favoring the coherent population in localized "islands" embedded in a "stochastic sea" [*Ashour-Abdalla et al.*, 1993, 1995, 2005]. The particles collected at our virtual spacecraft were injected from just a few, well-localized "active" sources, mainly because particles ejected from these sources reached an elongated "island" where $\kappa < 2$. The chosen source grid was relatively coarse, compared to the space scale of changes and shears in the local convection and, at that point, we cannot rule out that localized sources distributed on a finer MLT-ILAT grid would give higher contributions. Nevertheless, the main loss mechanisms from our sources are the very field-aligned population that is immediately lost in the conjugate hemisphere and those ions nonadiabatically trapped in the current sheet too long to return to the spacecraft in time.

[71] A second difference between data and simulations is related with the background noise. Because Cluster is located at $X \sim -3.8$, and is a distance $Z \sim +2.5$ R_E above the neutral sheet, a number of particles following cucumber orbits typical for the scattered population nevertheless reach the Cluster altitude in the simulations in a randomized way, i.e., unlike the accelerated particles, without coherence between their energy and their returning latitude. A careful selection of the sources would improve the signal-to-noise ratio of the structures, but to the detriment of the total number of collected particles.

[72] The third discrepancy is related with the low simulated flux for structures E3 and E4 compared to the experimental flux. The maximum energy flux detected by SC1 in structures E3 and E4 reaches $\sim 10^8$ keV/cm^2.s.sr, i.e., two times higher than the maximum flux in structures E1 and E2. This ratio is even higher, 4–5, when detected by SC3. Simulations indicate that the initial beam population is gradually scattered during each subsequent interaction with the current sheet, explaining why the detected flux is decreasing from one simulated structure to the next one. Moreover, in the simulations, higher order families were underestimated because many of the particles only counted within "1H0F" family, in fact would mirror and continue their bouncing motion to be also detected later on in subsequent families. However, this simple behavior could be changed by modulating in time the source outflow. We have noticed that the relative number of particles within each family is time-dependent and a drastic increase at 0302 UT of the outflow would greatly increase the relative number of 0H1F and 1H1F particles contributing to the E3 structure. Simulations show that a part of the 1H1F family (in reality evolving as 0H2F particles) coincides in latitude and energy (but not in flux) with the E4 structure. This structure has peculiar experimental properties: its $1/V$-latitude dispersion slope is smaller than the slope of the neighboring E3 structure (see Figure 7), and its distribution functions are highly collimated (see Figure 3c3) indicating perhaps a more "local" source. We also note that a <100 eV low-energy ionospheric outflow was detected by SC3 around 0311–0312 UT (Figure 3b3), but the upflowing flux seems insufficient to generate the E4 structure. This source, an additional (undetected) ionospheric source in the conjugate hemisphere, ionospheric O^+ ions, or the classic plasma mantle/stochastic sea could all possibly contribute to the robustness of the E4 structure.

6.2. Simple Modeling of Bouncing Echoes

[73] In order to determine the origin of the dispersed ion structures, *Bosqued et al.* [2006] presented a highly simplified model in which the $\mathbf{E} \times \mathbf{B}$ latitudinal drift of bouncing echoes was computed, assuming a constant poleward convection V_p, a field line of constant length l, and an *ad hoc* systematic acceleration each time the particle crossed the neutral sheet. In this simplistic case the dispersion in latitude, Λ_n (V_n) $-$ Λ_0 after n full bounces for a particle of final velocity V_n, is proportional to $(n.V_p.l)/V_n$, when uncorrected by terms related to the acceleration and/or changes in the field line length. Based on these hypotheses, the energy-latitude contours of the first two echoes were remarkably faithfully reproduced, but the origin of E1 and E2 was erroneously attributed to 1 full bounce and 2 full bounce particles [*Bosqued et al.*, 2006]. *Bosqued et al.* assumed a field line half-length of 13 R_E (or a distance of the spacecraft to the neutral sheet of $\sim$9.5 R_E along the field line), and a negligible time spent in the neutral sheet acceleration region; more importantly, half bouncing particles were not envisaged. Figure 13a indicates that the half-bounce length (from the spacecraft position to the neutral sheet) is considerably longer, $\sim$18–19 R_E, mainly because the MHD field lines are stretched. If this hypothesis is used, formula (1) by *Bosqued et al.* [2006] would correctly attribute the echo E1 to half-bouncing particles. The same reasoning could be applied to 1H0Fb and 0H1F particles (Figures 13b and 13c): again, the twice longer field line length than that anticipated in the highly simplified calculations, the same time-of-flight, of the order of 7 min, and these two populations will mix to coincide with the E2 echo, which was misinterpreted as a second full-bounce echo by *Bosqued et al.* [2006]. When the oversimplified calculations are corrected, the simple time-of-flight arguments do not disagree with the simulations presented here.

6.3. Weaknesses of Alternative Interpretations

[74] We must justify why an alternate hypothesis, attributing the observed ion structures to velocity dispersed ion structures (VDIS) related to PSBL beams, is inconsistent with the observed properties. Discovered by the Aureol-3 spacecraft [*Bosqued*, 1987], and first described and interpreted by *Zelenyi et al.* [1990] and *Bosqued et al.* [1993], VDIS are the auroral counterpart of PSBL beams observed downtail [*Takahashi and Hones*, 1988]. At midaltitude and low altitudes, VDIS are characterized by ions that have highest energies near the polar cap boundary, and a decreasing energy with decreasing latitude. We in fact began this study by first adopting the current view of a tail origin, and exactly followed the method used in simulating the 14 February 2001 southern hemisphere event (detected 2 hours before the present event), and interpreted as a VDIS by *Keiling et al.* [2004a, 2004b]. For this first event, *Ashour-Abdalla et al.* [2005] traced VDIS ions backward in time and found that the VDIS were generated in a region of nonadiabatic motion just earthward of the neutral line called the "stochastic sea." A backward-tracing study proved unfruitful for the present event, because ions unexpectedly drifted equatorward, and not poleward, and

reached the ionosphere equatorward of the E1 ramp. That was a sufficient reason to start the search a local source, found at the exact location reached by backward-traced ions.

[75] After studying tens of events, *Zelenyi et al.* [1990] and *Bosqued et al.* [1993] established that a conjunction of simple properties must be fulfilled to correctly infer that the ion beams observed at mid or low altitudes can be correctly interpreted as VDIS originating at the distant tail source. Such properties, not contradicted by all results accumulated since 1990, are (1) the highest energy part of VDIS is always confined to a narrow region at $\leq 0.4°$ ILAT near this polar cap boundary, and (2) the dispersive relationship between the energy W and latitude Λ is always of the form $W \propto 1/(\Lambda_{pc} - \Lambda)^2$, where Λ_{pc} is the latitude of the polar cap boundary. We have shown in section 4.3 that the polar cap boundary is located at $\sim 76°$ ILAT, i.e., more than $1°$ poleward of the polewardmost ion structure, and not near this boundary, which can be erroneously identified when only ion data are used. Moreover, the polar diffuse zone of soft electron precipitation often associated with the PSBL [*Galperin and Feldstein*, 1989] is clearly evident during the present event, well poleward of the ion structures. The second argument, even more discriminating, is related with the observed dispersion. *Zelenyi et al.* [1990] explained that the dispersion may result from two additional effects: (1) the $\mathbf{E} \times \mathbf{B}$ velocity filter effect, and (2) a source distributed along the X direction downtail. As the $B_z(X)$ local component of the magnetic field controls the local ion acceleration, variations of B_z along X will also control the dispersion. *Zelenyi et al.* [1990] showed that all realistic $B_z(X)$ profiles give a final energy dispersion of the above form, fully confirmed by successive simulations, starting from very simple two-dimensional models [*Ashour-Abdalla et al.*, 1992] to the most recent three-dimensional models [*Ashour-Abdalla et al.*, 2008]. A similar dispersion is correctly followed by the unambiguous Cluster VDIS events [e.g., *Keiling et al.*, 2004a, 2004b], even if substructures (beamlets) follow different dispersions, and by PSBL beams observed at $X \sim -16$ R_E downtail by Cluster [*Ashour-Abdalla et al.*, 2008]. Coming back to the present event, Figure 7 has clearly demonstrated that neither the average profile of the ion structures nor the maximum or minimum energy profiles, can be fitted by the expected law; instead of an hyperbolic variation up to the asymptotic polar cap boundary Λ_{pc}, the energy is linearly increasing with latitude, $W \propto \Lambda$.

[76] Although the above arguments should be sufficient to reject a downtail origin for the observed structures, we explore another possibility, namely that successive dispersed structures could be signatures of PSBL oscillations and flapping. A number of past studies [*Parks et al.*, 1998; *Möbius et al.*, 1983; *Andrews et al.*, 1981; *Forbes et al.*, 1981; *Eastman et al.*, 1985; *Ashour-Abdalla et al.*, 1995] demonstrated that the plasma sheet is moving mainly along Z with velocities ranging from 10 to 60 km/s. This fast motion, compared to the slow motion of a spacecraft near its apogee, has been used to infer local PSBL Z profiles, in the past with the ISEE spacecraft [*Takahashi and Hones*, 1988; *Parks et al.*, 1998] and also very recently with Cluster [*Ashour-Abdalla et al.*, 2008]. The typical signature observed by the spacecraft takes the form of successive energy increases and decreases of the beam energy with time, correlated with successive PSBL thinnings/thickenings, with a periodicity of ~ 10 minutes. Of course, structures with decreasing energy profiles can be generated in this manner, but will be immediately coupled with the reverse energy structure of about the same duration and the same slope [see *Ashour-Abdalla et al.*, 2008]. We rule out such oscillations as a possible interpretation of the dispersed structures observed on 14 February 2001 for at least two reasons: (1) as shown in Figures 2 and 6, there is absolutely no evidence for oscillations in the multispacecraft electron and magnetic field Cluster data, nor in the IMAGE data, and (2) the positive energy-latitude structures are not present at all, and the SC1 and SC3 variations are absolutely not synchronous, as needed if resulting from PSBL oscillations. In order to definitively reject this hypothesis, a further argument is provided by the orderly changes in the slopes of the successive structures E1, E2, E3, and E4 presented in Figure 7. It is difficult to imagine such coherent and orchestrated changes in the PSBL flapping motion velocity.

[77] This exciting event was previously analyzed by *Keiling et al.* [2004a]. First, the authors interpreted the successively observed structures (assumed to be separated in time, not latitude) as signatures of ion beamlets ejected from localized sources distributed between $X \sim -70$ and ~ -110 R_E along the distant tail. However, these results were obtained by eyeball-fitting the Cluster spectrograms [*Keiling et al.*, 2004a], a much less accurate method than the convergent fittings presented in Figure 7. Moreover, the reported downtail distances are inconsistent with our MHD results where the neutral line is not rejected far in the tail, but is only $30-40$ R_E downtail (see Figure 9). Second, the authors rely on the hypothesis that successive dispersions are definitively time dispersions. To interpret this event *Keiling et al.* [2004a] invoked a scenario that mixes temporal and spatial effects, without a firm basis in observations, and without the benefit of global modeling. This scenario assumes an unrealistic coherent activity "orchestration," in which (1) an exact time synchronization is required for the impulsive time switch on/off of each of the three to four isolated current sheet sources, and (2) requires an additional, but improbable, phasing with the Cluster orbit, in which spacecraft must be located at the correct time and correct location to collect ion beamlets. However, *Keiling et al.* [2004a] correctly noted that spatial effects were also evident, as the same ion structures were crossed at different times by the successive SC1–SC3 satellites. To account for the observed time shift between SC1 and SC3 observations, an additional equatorward convection of the flux tubes was arbitrarily (and erroneously) suggested.

[78] Although not explicitly invoked, the idea supported by *Keiling et al.* [2004a] is that each individual source could be the tail-distributed "resonant" sources predicted by *Ashour-Abdalla et al.* [1995]. *Sauvaud and Kovrazhkin* [2004] duplicated the same interpretation of the present event, but explicitly suggested this resonant effect. The low-altitude signature of resonances could be the small-scale structures called "beamlets," first modeled by *Ashour-Abdalla et al.* [1992] and observed at low altitudes by *Bosqued et al.* [1993]. More recently, a very nice beamlet event, which also included echoes, was observed by Cluster [*Keiling et al.*, 2004b]. These echoes, or subsequent bouncing beamlets, were also predicted by *Ashour-Abdalla et al.*

[1992] and previously observed by *Bosqued et al.* [1993]. These last *Keiling et al*. observations were recently and nicely modeled by *Ashour-Abdalla et al.* [2005]. Surprisingly, the possibility of echoes did not appear in the complementary interpretations of the present event published by *Keiling et al.* [2004a] and *Sauvaud and Kovrazhkin* [2004]. Both papers presumably kept in mind the classical view (see below), in which the $\mathbf{E} \times \mathbf{B}$ drift is directed equatorward and disperses echoes equatorward of the original "beamlets." Similarly, the authors clearly had trouble coming up with a mechanism that would precipitate lower energy ions further poleward than high-energy ones. It is generally anticipated that, during outbound crossings (from the equatorial plane to the northern lobe), due to the presumably equatorward $\mathbf{E} \times \mathbf{B}$ drift motion, the related energy-latitude dispersion is the reverse of a pure time-of-flight dispersion, in which higher energy ions are precipitated first. Thus we concede that, in the absence of careful analysis of convection data it is tempting to interpret the successive energy ramps (like those observed by Cluster during the present event) as energy-time dispersions. Accordingly, the weaker point of the invalid interpretations of *Keiling et al.* [2004a] and *Sauvaud and Kovrazhkin* [2004], again repeated and attributed to pure temporal effects in *Sharma et al.* [2008], is their incomplete analysis of the available data, and, particularly, their failure to discern the two key Cluster observations revealed in this paper: (1) the presence of an intense ionospheric source, just equatorward of the dispersed structures, and (2) unexpected localized poleward convection.

6.4. Concluding Remarks

[79] In conclusion, this joint experimental/numerical study demonstrates the relation existing between successive energy-dispersed ion structures and a local ionospheric source of outflowing field-aligned H^+ ion beams. Ion data accumulated from three Cluster spacecraft unambiguously demonstrate that the ionospheric energetic outflow persisted for minutes in a narrow auroral arc. LSK simulations lead to the generation of successive energy-dispersed substructures that are nothing more than a combination of half-bouncing and bouncing echoes (after ½ bounce, 1 bounce, 1½ bounces, 2 bounces, ...), of the ionospheric source. It is notable that unexpected half-bounce accelerated echoes have, for the first time in bouncing ion studies, been detected and simulated. The unusual poleward latitudinal dispersion is shown to result from the $\mathbf{E} \times \mathbf{B}$ filter effect in a narrow channel in which the local convection is directed tailward in the magnetotail (or poleward in the ionosphere). The MHD model correctly models this local channel of tailward convecting flow in the midnight sector, in the vicinity of Cluster magnetic field lines, persisting for the entire interval of interest, in agreement with the poleward flows measured by all the Cluster spacecraft. As predicted by more simplistic two-dimensional, time-independent models [*Ashour-Abdalla et al.*, 1992], a majority of ions were nonadiabatically accelerated each time they encountered the neutral sheet. The present simulations quantify this energy gain amount as ~2–5 keV or even more per interaction. The observed increase in energy, from one structure to the next, naturally results from additive nonadiabatic acceleration impulses of several keV occurring when particles interact with the current sheet. Our MHD + LSK simulations show that this interaction occurs along a narrow and elongated "island," not too far along the tail but nevertheless on stretched field lines prevailing at or near the vortex of tailward convection. The MHD code predicts changes in the magnetic and electric field over a time period of ~1 min, and these changes may affect the details of successive echoes, e.g., reaching higher energies, and returning positions and times. Additional scattering was evident in the equatorial plane in relation to the stochastic interaction, precluding or, at the very least, making it difficult for the ions to return to the correct location along the satellite track. Nevertheless, for particles returning back to the northern ionosphere, the spread is of the order of 1–2H MLT in azimuth, westward of the original source, much less than anticipated. In spite of these changes, the energy-dispersed structures are relatively robust, even though the initial beams survive in the simulations only through a limited number of crossings, probably four or five interactions.

[80] Although an a priori tendency would be to interpret this event as a succession of VDIS time-dispersed beamlets, MHD + LSK simulations have been essential for the full understanding of this unique event in which the ion source was, for the first time, observed in conjunction with successive bouncing echoes. Very strong constraints were imposed, on time-dependent modeling of the nightside magnetosphere, on the particle tracking through varying magnetic and electric fields, and on particle nonadiabatic acceleration. Many intriguing features have been revealed for the first time, as the detection and simulation of unexpected half-bounce accelerated echoes and their higher-order multiple echoes. This discovery, associated to the confirmed importance of the ionospheric ion source, should encourage new multipoint studies of multiple bouncing ion clusters within the magnetosphere.

[81] **Acknowledgments.** We thank CDAWeb and D. J. McComas (SWRI), R. Lepping (NASA/GSFC) for providing CDAWeb with key parameters of the ACE magnetic field and plasma instruments. The AE index was provided by WDC-2 in Kyoto. The Cluster data have been kindly provided by H. Rème (CIS), M. Dunlop (FGM), A. Fazakerley (PEACE), G. Paschmann (EDI), and P. Daly (RAPID). We thank the OVT Team (http://ovt.irfu.se) for allowing us to use the Orbit Visualization Tools. The authors thank Ray Walker for his helpful comments and Heinz Kohne for his assistance in computing and production. Work at CESR/CNRS was funded by CNES (French Space Agency). Research at UCLA was supported by NASA grant NNG05GG58G. Computing support was provided by NASA Advanced Supercomputing Division's Columbia Supercomputer.

[82] Amitava Bhattacharjee thanks Toshifumi Mukai and two other reviewers for their assistance in evaluating this paper.

References

Andrews, M. K., E. Keppler, and P. W. Daly (1981), Plasma sheet motions inferred from medium-energy ion measurements, *J. Geophys. Res.*, *86*(A9), 7543–7556.

Ashour-Abdalla, M., L. M. Zelenyi, J. M. Bosqued, and R. A. Kovrazhkin (1992), Precipitation of fast ion beams from the plasma sheet boundary layer, *Geophys. Res. Lett.*, *19*(6), 617–620.

Ashour-Abdalla, M., J. P. Berchem, J. Büchner, and L. M. Zelenyi (1993), Shaping of the magnetotail from the mantle: Global and local structuring, *J. Geophys. Res.*, *98*(A4), 5651–5676.

Ashour-Abdalla, M., L. M. Zelenyi, V. Peroomian, and R. L. Richard (1994), Consequences of magnetotail ion dynamics, *J. Geophys. Res.*, *99*(A8), 14,891–14,916.

Ashour-Abdalla, M., L. M. Zelenyi, V. Peroomian, R. L. Richard, and J. M. Bosqued (1995), The mosaic structure of plasma bulk flows in the Earth's magnetotail, *J. Geophys. Res.*, *100*(A10), 19,191–19,209.

Ashour-Abdalla, M., et al. (1997), Ion sources and acceleration mechanisms inferred from local distribution functions, *Geophys. Res. Lett.*, *24*(8), 955–958.

Ashour-Abdalla, M., M. El-Alaoui, V. Peroomian, R. J. Walker, L. M. Zelenyi, L. A. Frank, and W. R. Paterson (1999), Localized reconnection and substorm onset on Dec. 22, 1996, *Geophys. Res. Lett.*, *26*(23), 3545–3548.

Ashour-Abdalla, M., M. El-Alaoui, V. Peroomian, R. J. Walker, J. Raeder, L. A. Frank, and W. R. Paterson (2000), The origin of the near-Earth plasma population during a substorm on November 24, 1996, *J. Geophys. Res.*, *105*(A2), 2589–2605.

Ashour-Abdalla, M., M. El-Alaoui, F. V. Coroniti, R. J. Walker, and V. Peroomian (2002), A new convection state at substorm onset: Results from an MHD study, *Geophys. Res. Lett.*, *29*(20), 1965, doi:10.1029/2002GL015787.

Ashour-Abdalla, M., J. M. Bosqued, M. El-Alaoui, V. Peroomian, L. M. Zelenyi, R. J. Walker, and J. Wright (2005), A stochastic sea: The source of plasma sheet boundary layer ion structures observed by Cluster, *J. Geophys. Res.*, *110*, A12221, doi:10.1029/2005JA011183.

Ashour-Abdalla, M., J. N. Leboeuf, D. Schriver, J.-M. Bosqued, N. Cornilleau-Wehrlin, V. Sotnikov, A. Marchaudon, and A. N. Fazakerley (2006), Instabilities driven by ion shell distributions observed by Cluster in the midaltitude plasma sheet boundary layer, *J. Geophys. Res.*, *111*, A10223, doi:10.1029/2005JA011490.

Ashour-Abdalla, M., J. M. Bosqued, M. El-Alaoui, V. Peroomian, T. Umeda, and R. J. Walker (2008), Modeling PSBL high speed ion beams observed by Cluster and double star, *J. Adv. Space Res.*, *41*(10), 1598–1610, doi:10.1016/j.asr.2007.04.018.

Balogh, A., et al. (2001), The Cluster magnetic field investigation: Overview of in-flight performance and initial results, *Ann. Geophys.*, *19*, 1207–1217.

Berchem, J., J. Raeder, M. Ashour-Abdalla, L. A. Frank, W. R. Paterson, K. L. Ackerson, S. Kokubun, T. Yamamoto, and R. P. Lepping (1998), The distant tail at 200 R_E: Comparison between Geotail observations and the results of global MHD simulation, *J. Geophys. Res.*, *103*(A5), 9121–9141.

Bosqued, J. M. (1987), AUREOL-3 results on ion precipitation, *Phys. Scripta*, *18*, 158–166.

Bosqued, J. M., J. A. Sauvaud, D. Delcourt, and R. A. Kovrazhkin (1986a), Precipitation of suprathermal ionospheric ions accelerated in the conjugate hemisphere, *J. Geophys. Res.*, *91*(A6), 7006–7018.

Bosqued, J. M., C. Maurel, J. A. Sauvaud, R. A. Kovrazhkin, and Y. I. Galperin (1986b), Observations of auroral electron inverted-V structures by the AUREOL-3 satellite, *Planet. Space Sci.*, *34*(3), 255–269.

Bosqued, J. M., M. Ashour-Abdalla, M. El Alaoui, V. Peroomian, L. M. Zelenyi, and C. P. Escoubet (1993), Dispersed ion structures at the poleward edge of the auroral oval: Low-altitude observations and numerical modeling, *J. Geophys. Res.*, *98*(A11), 19,181–19,204.

Bosqued, J. M., et al. (2006), Cluster observations of energetic ionospheric ion beams in the auroral region: Acceleration and associated energy-dispersed precipitation, *Geophys. Res. Lett.*, *33*, L12102, doi:10.1029/2006GL025708.

Boyle, C. B., P. H. Reiff, and M. R. Hairston (1997), Empirical polar cap potentials, *J. Geophys. Res.*, *102*(A1), 111–126.

Büchner, J., and L. M. Zelenyi (1986), Deterministic chaos in the dynamics of charged particle near a magnetic field reversal, *Phys. Lett. A*, *118*(8), 395–399.

Büchner, J., and L. M. Zelenyi (1989), Regular and chaotic charged particle motion in magnetotail-like field reversals: 1. Basic theory of trapped motion, *J. Geophys. Res.*, *94*(A9), 11,821–11,842.

Birn, J., and M. Hesse (1991), MHD simulations of magnetic reconnection in a skewed three-dimensional tail configuration, *J. Geophys. Res.*, *96*(A1), 23–34.

Birn, J., E. W. Hones Jr., and K. Schindler (1986), Field-aligned plasma flow in MHD simulations of magnetotail reconnection and the formation of boundary layers, *J. Geophys. Res.*, *91*(A10), 11,116–11,122.

Chiu, Y. T., and M. Schulz (1978), Self-consistent particle and parallel electrostatic field distributions in the magnetospheric-ionospheric auroral region, *J. Geophys. Res.*, *83*(A2), 629–642.

Cowley, S. W. H. (1980), Plasma populations in a simple open model magnetosphere, *Space Sci. Rev.*, *26*, 217–275.

DeCoster, R. J., and L. A. Frank (1979), Observations pertaining to the dynamics of the plasma sheet, *J. Geophys. Res.*, *84*(A9), 5099–5121.

Eastman, T. E., L. A. Frank, W. K. Peterson, and W. Lennartsson (1984), The plasma sheet boundary layer, *J. Geophys. Res.*, *89*(A3), 1553–1572.

Eastman, T. E., L. A. Frank, and C. Y. Huang (1985), The boundary layers as the primary transport regions of the Earth's magnetotail, *J. Geophys. Res.*, *90*(A10), 9541–9560.

El-Alaoui, M. (2001), Current disruption during November 24, 1996, substorm, *J. Geophys. Res.*, *106*(A4), 6229–6245.

El-Alaoui, M., M. Ashour-Abdalla, J. M. Bosqued, and R. L. Richard (2008), Understanding magnetotail current sheet meso-scale structures using MHD simulations, *Adv. Space Res.*, *41*, 1630–1642, doi:10.1016/j.asr.2007.05.061.

Elphinstone, R. D., D. J. Hearn, L. L. Cogger, J. S. Murphree, A. Wright, I. Sandahl, S. Ohtani, P. T. Newell, D. M. Klumpar, and M. Shapshak (1995), The double oval UV auroral distribution: 2. The most poleward arc system and the dynamics of the magnetotail, *J. Geophys. Res.*, *100*(A7), 12,093–12,102.

Feldstein, Y. I., and Yu. I. Galperin (1985), The auroral luminosity structure in the high-latitude upper atmosphere: Its dynamics and relationship to the large-scale structure of the Earth's magnetosphere, *Rev. Geophys.*, *23*(3), 217–275.

Forbes, T. G., E. W. Hones Jr., S. J. Bame, J. R. Asbridge, G. Paschmann, N. Sckopke, and C. T. Russell (1981), Substorm-related plasma sheet motions as determined from differential timing of plasma changes at the Isee satellites, *J. Geophys. Res.*, *86*(A5), 3459–3469.

Frey, H. U., S. B. Mende, C. W. Carlson, J.-C. Gérard, B. Hubert, J. Spann, R. Gladstone, and T. J. Immel (2001), The electron and proton aurora as seen by IMAGE-FUV and FAST, *Geophys. Res. Lett.*, *28*(6), 1135–1138.

Frey, H. U., S. B. Mende, T. J. Immel, J.-C. Gérard, B. Hubert, S. Habraken, J. Spann, G. R. Gladstone, D. V. Bisikalo, and V. I. Shematovich (2003), Summary of quantitative interpretation of IMAGE far ultraviolet auroral data, *Space Sci. Rev.*, *109*, 255–283.

Galperin, Yu. I., and Y. I. Feldstein (1989), Auroral luminosity and its relationship to magnetospheric plasma domains, in *Auroral Physics*, edited by C. I. Meng, Cambridge Univ. Press, New York.

Ghielmetti, A. G., R. G. Johnson, R. D. Sharp, and E. G. Shelley (1978), The latitudinal, diurnal, and altitudinal distributions of upward flowing energetic ions of ionospheric origin, *Geophys. Res. Lett.*, *5*(1), 59–62.

Gustafsson, G., et al. (2001), First results of electric field and density observations by Cluster EFW based on initial months of operation, *Ann. Geophys.*, *19*, 1219–1240.

Hasegawa, A. (1987), Beam production at plasma boundries by kinetic Alfvén waves, *J. Geophys. Res.*, *92*(A10), 11,221–11,223.

Hirahara, M., T. Mukai, T. Nagai, N. Kaya, H. Hayakawa, and H. Fukunishi (1996), Two types of ion energy dispersions observed in the nightside auroral regions during geomagnetically disturbed periods, *J. Geophys. Res.*, *101*(A4), 7749–7767.

Hirahara, M., T. Mukai, E. Sagawa, N. Kaya, and H. Hayakawa (1997), Multiple energy-dispersed ion precipitations in the low-latitude auroral oval: Evidence of E × B drift effect and upward flowing ion contribution, *J. Geophys. Res.*, *102*(A2), 2513–2530.

Janhunen, P., A. Olsson, A. Vaivads, and W. K. Peterson (2003), Generation of Bernstein waves by ion shell distribution in the auroral region, *Ann. Geophys.*, *21*, 881–891.

Johnstone, A. D., et al. (1997), PEACE: A plasma electron and current experiment, *Space Sci. Rev.*, *79*, 351–398.

Kazama, Y., and T. Mukai (2003), Multiple energy-dispersed ion signatures in the near-Earth magnetotail: Geotail observation, *Geophys. Res. Lett.*, *30*(7), 1384, doi:10.1029/2002GL016637.

Kazama, Y., and T. Mukai (2005), Simultaneous appearance of energy-dispersed ion signatures of ionospheric and magnetotail origins in the near-Earth plasma sheet, *J. Geophys. Res.*, *110*, A07213, doi:10.1029/2004JA010820.

Keiling, A., et al. (2004a), Transient ion beamlet injections into spatially separated PSBL flux tubes observed by Cluster-CIS, *Geophys. Res. Lett.*, *31*, L12804, doi:10.1029/2004GL020192.

Keiling, A., et al. (2004b), New properties of energy-dispersed ions in the plasma sheet boundary layer observed by Cluster, *J. Geophys. Res.*, *109*, A05215, doi:10.1029/2003JA010277.

Keiling, A., et al. (2005), Bouncing ion clusters in the plasma sheet boundary layer observed by Cluster-CIS, *J. Geophys. Res.*, *110*, A09207, doi:10.1029/2004JA010497.

Klumpar, D. M. (1979), Transversely accelerated ions: An ionospheric source of hot magnetospheric ions, *J. Geophys. Res.*, *84*(A8), 4229–4237.

Kondo, T., B. A. Whalen, A. W. Yau, and W. K. Peterson (1990), Statistical analysis of upflowing ion beam and conic distributions at DE1 altitudes, *J. Geophys. Res.*, *95*(A8), 12,091–12,102.

Kullen, A., J. A. Cumnock, and T. Karlsson (2008), Seasonal dependence and solar wind control of transpolar arc luminosity, *J. Geophys. Res.*, *113*, A08316, doi:10.1029/2008JA013086.

Lennartsson, O. W., K. J. Trattner, H. L. Collin, and W. K. Peterson (2001), Polar/toroidal imaging mass-angle spectrograph survey of earthward field-aligned proton flows from the near-midnight tail, *J. Geophys. Res.*, *106*(A4), 5859–5871.

Lyons, L. R., and T. W. Speiser (1982), Evidence for current sheet acceleration in the geomagnetic tail, *J. Geophys. Res.*, *87*(A4), 2276–2286.

Lyons, L. R., and D. J. Williams (1984), *Quantitative Aspects of Magnetospheric Physics*, Springer, New York.

Marklund, G. (1993), Viking investigations of auroral electrodynamical processes, *J. Geophys. Res.*, *98*(A2), 1691–1704.
Mende, S. B., et al. (2000), Far ultraviolet imaging from the IMAGE spacecraft: 3. Spectral imaging of Lyman a and OI 135.6 nm, *Space Sci. Rev.*, *91*, 287–318, doi:10.1023/A:1005271728567.
McFadden, J. P., et al. (1998), Spatial structure and gradients of ion beams observed by FAST, *Geophys. Res. Lett.*, *25*(12), 2021–2024.
Möbius, E., F. M. Ipavich, M. Scholer, G. Gloeckler, D. Hovestadt, and B. Klecker (1980), Observations of a nonthermal ion layer at the plasma sheet boundary layer, *J. Geophys. Res.*, *85*(A10), 5143–5148.
Möbius, E., M. Scholer, D. Hovestadt, G. Paschmann, and G. Gloeckler (1983), Energetic particles in the vicinity of a possible neutral line in the plasma sheet, *J. Geophys. Res.*, *88*(A10), 7742–7752.
Moghaddam-Taaheri, E., C. K. Goertz, and R. A. Smith (1991), Plasma convection and ion beam generation in the plasma sheet boundary layer, *J. Geophys. Res.*, *96*(A2), 1569–1583.
Mozer, F. S., C. A. Cattell, M. K. Hudson, R. L. Lysak, M. Temerin, and R. B. Torbert (1980), Satellite measurements and theories of low altitude auroral particle acceleration, *Space Sci. Rev.*, *27*, 155–213.
Parks, G., L. J. Chen, M. McCarthy, D. Larson, R. P. Lin, T. Phan, H. Reme, and T. Sanderson (1998), New observations of ion beams in the plasma sheet boundary layer, *Geophys. Res. Lett.*, *25*(17), 3285–3288.
Paschmann, G., et al. (2001), The electron drift instrument on Cluster: Overview of first results, *Ann. Geophys.*, *19*, 1273–1288.
Peroomian, V., M. El-Alaoui, M. Ashour-Abdalla, and L. M. Zelenyi (2007), A comparison of solar wind and ionospheric plasma contributions to the September 24–25, 1998 magnetic storm, *J. Atm. Terrest. Phys.*, *69*(3), 189–402.
Popescu, D., J.-A. Sauvaud, H. Stenuit, D. C. Delcourt, V. A. Sergeev, M. Brittnacher, G. K. Parks, T. Mukai, S. Kokubun, and R. A. Kovrazhkin (2002), Auroral signatures of transient processes in the outer magnetosphere, *Adv. Space Res.*, *30*, 2701–2711.
Quinn, J. M., and C. E. McIlwain (1979), Bouncing ion clusters in the Earth's magnetosphere, *J. Geophys. Res.*, *84*(A12), 7365–7370.
Quinn, J. M., and D. J. Southwood (1982), Observations of parallel ion energization in the equatorial region, *J. Geophys. Res.*, *87*(A12), 10,536–10,540.
Raeder, J., R. J. Walker, and M. Ashour-Abdalla (1995), The structure of the distant geomagnetic tail during long periods of northward IMF, *Geophys. Res. Lett.*, *22*(4), 349–352.
Raeder, J., J. Berchem, and M. Ashour-Abdalla (1998), The geospace environment modeling grand challenge: Results from a global geospace circulation model, *J. Geophys. Res.*, *103*(A7), 14,787–14,798.
Reiff, P. H., H. L. Collin, E. G. Shelley, J. L. Burch, and J. D. Winningham (1986), Heating of upflowing ionospheric ions on auroral field lines, in *Ion Acceleration in the Magnetosphere and Ionosphere*, *Geophys. Monogr. Ser.*, vol. 38, edited by T. Chang, p. 83, AGU, Washington, D. C.
Reiff, P. H., H. L. Collin, J. D. Craven, J. L. Burch, J. D. Winningham, E. G. Shelley, L. A. Frank, and M. A. Friedman (1988), Determination of auroral electrostatic potentials using high- and low-altitude particle distributions, *J. Geophys. Res.*, *93*(A7), 7441–7465.
Rème, H., C. Aoustin, J. M. Bosqued, and I. Dandouras (2001), First multispacecraft ion measurements in and near the Earth's magnetosphere with the identical Cluster ion spectrometry (CIS) experiment, *Ann. Geophys.*, *19*, 1303–1354.
Ruohoniemi, J. M., and K. B. Baker (1998), Large-scale imaging of high-latitude convection with Super Dual Auroral Radar Network HF radar observations, *J. Geophys. Res.*, *103*(A9), 20,797–20,811.
Sauvaud, J.-A., and R. A. Kovrazhkin (2004), Two types of energy-dispersed ion structures at the plasma sheet boundary, *J. Geophys. Res.*, *109*, A12213, doi:10.1029/2003JA010333.
Sauvaud, J.-A., D. Popescu, D. C. Delcourt, G. K. Parks, M. Brittnacher, V. Sergeev, R. A. Kovrazhkin, T. Mukai, and S. Kokubun (1999), Sporadic plasma sheet ion injections into the high-altitude auroral bulge: Satellite observations, *J. Geophys. Res.*, *104*(A12), 28,565–28,586.
Scarf, F. L., R. W. Fredricks, C. T. Russell, M. Kivelson, M. Neugebauer, and C. R. Chappell (1973), Observation of a current-driven plasma instability at the outer zone-plasma sheet boundary, *J. Geophys. Res.*, *78*(13), 2150–2165.
Schindler, K., and J. Birn (1987), On the generation of field-aligned plasma flow at the boundary of the plasma sheet, *J. Geophys. Res.*, *92*(A1), 95–107.
Schriver, D., M. Ashour-Abdalla, R. J. Strangeway, R. L. Richard, C. Klezting, Y. Dotan, and J. Wygant (2003), FAST/Polar conjunction study of field-aligned auroral acceleration and corresponding magnetotail drivers, *J. Geophys. Res.*, *108*(A9), 8020, doi:10.1029/2002JA009426.
Sharma, A. S., et al. (2008), Transient and localized processes in the magnetotail: A review, *Ann. Geophys.*, *26*, 955–1006.
Shelley, E. G., R. G. Johnson, and R. D. Sharp (1972), Satellite observations of energetic heavy ions during a geomagnetic storm, *J. Geophys. Res.*, *77*(31), 6104–6110.
Shelley, E. G., R. D. Sharp, and R. G. Johnson (1976), Satellite observations of an ionospheric acceleration mechanism, *Geophys. Res. Lett.*, *3*(11), 654–656.
Speiser, T. W. (1965), Particle trajectories in the model current sheets: 1. Analytical solutions, *J. Geophys. Res.*, *70*(17), 4219–4226.
Speiser, T. W. (1968), On the uncoupling of parallel and perpendicular particle motion in a neutral sheet, *J. Geophys. Res.*, *73*(3), 1112–1113.
Takahashi, K., and W. Hones Jr. (1988), ISEE 1 and 2 observations of ion distributions at the plasma sheet-tail lobe boundary, *J. Geophys. Res.*, *93*(A8), 8558–8582.
Tsyganenko, N. A. (1989), A magnetospheric magnetic field model with a warped tail current sheet, *Planet. Space Sci.*, *37*, 5–20.
Tsyganenko, N. A. (2002a), A model of the near magnetosphere with a dawn-dusk asymmetry: 1. Mathematical structure, *J. Geophys. Res.*, *107*(A8), 1179, doi:10.1029/2001JA000219.
Tsyganenko, N. A. (2002b), A model of the near magnetosphere with a dawn-dusk asymmetry: 2. Parameterization and fitting to observations, *J. Geophys. Res.*, *107*(A8), 1176, doi:10.1029/2001JA000220.
Walker, R. J., M. Ashour-Abdalla, M. El Alaoui, and F. V. Coroniti (2006), Magnetospheric convection during prolonged intervals with southward interplanetary magnetic field, *J. Geophys. Res.*, *111*, A10219, doi:10.1029/2005JA011541.
Whalen, B. A., W. Bernstein, and P. W. Daly (1978), Low altitude acceleration of ionospheric ions, *Geophys. Res. Lett.*, *5*(1), 55–58.
Williams, D. J. (1981), Energetic ion beams at the edge of the plasma sheet: ISEE 1 observations plus a simple explanatory model, *J. Geophys. Res.*, *86*(A7), 5507–5518.
Winningham, J. D., J. L. Burch, and R. A. Frahm (1984), Bands of ions and angular V's: A conjugate manifestation of ionospheric ion acceleration, *J. Geophys. Res.*, *89*(A3), 1749–1754.
Yau, A. W., B. A. Whalen, W. K. Peterson, and E. G. Shelley (1984), Distribution of upflowing ionospheric ions in the high-altitude polar cap and auroral ionosphere, *J. Geophys. Res.*, *89*(A7), 5507–5522.
Zelenyi, L. M., R. A. Kovrazhkin, and J. M. Bosqued (1990), Velocity dispersed ion beams in the nightside auroral zone: AUREOL 3 observations, *J. Geophys. Res.*, *95*(A8), 12,119–12,139.

M. Ashour-Abdalla, M. El Alaoui, and V. Peroomian, Institute of Geophysics and Planetary Physics, University of California, 405 Hilgard Avenue, Los Angeles, CA 90095-1567, USA. (mabdalla@igpp.ucla.edu; mostafa@igpp.ucla.edu; vahe@igpp.ucla.edu)

J. M. Bosqued, Centre d'Etude Spatiale des Rayonnements, Centre National de la Recherche Scientifique, CNRS, BP 4346, F-31028 Toulouse Cedex 4, France. (bosqued@cesr.fr)

H. U. Frey, Space Sciences Laboratory, University of California, Grizzly Peak Boulevard, Berkeley, CA 94720, USA. (hfrey@ssl.berkeley.edu)

H. Laakso, Space Science Department, European Space Research and Technology Centre, European Space Agency, Postbus 299, Keplerlaan, 1, NL-2200 AG Noordwijk, Netherlands. (harri.laakso@esa.int)

A. Marchaudon, Laboratoire de Physique et Chimie de l'Environnement, Centre National de la Recherche Scientifique, 3A, Av. de la Recherche Scientifique, F-45071 Orleans Cedex 2, France. (aurelie.marchaudon@cnrs-orleans.fr)

T. Umeda, Geospace Research Center, Solar-Terrestrial Environment Laboratory, Nagoya University, Nagoya, Aichi 464-8601, Japan. (umeda@stelab.nagoya-u.ac.jp)